VLBI for Gravity Probe B. II. Monitoring of the Structure of the Reference Sources 3C 454.3, B2250+194, and B2252+172

The Astrophysical Journal Supplement Series, 201:2 (29pp), 2012 July doi:10.1088/0067-0049/201/1/2

VLBI FOR *GRAVITY PROBE B*. II. MONITORING OF THE STRUCTURE OF THE REFERENCE SOURCES 3C 454.3, B2250+194, AND B2252+172

R. R. Ransom[1,4], N. Bartel[1], M. F. Bietenholz[1,5], D. E. Lebach[2],
J. I. Lederman[3], P. Luca[1], M. I. Ratner[2], and I. I. Shapiro[2]
[1] Department of Physics and Astronomy, York University, 4700 Keele Street, Toronto, ON, M3J 1P3, Canada
[2] Harvard-Smithsonian Center for Astrophysics, 60 Garden Street, Cambridge, MA 02138, USA
[3] Centre for Research in Earth and Space Sciences, York University, 4700 Keele Street, Toronto, ON M3J 1P3, Canada
Received 2011 May 31; accepted 2011 December 16; published 2012 June 7

ABSTRACT

We used 8.4 GHz very long baseline interferometry images obtained at up to 35 epochs between 1997 and 2005 to examine the radio structures of the main reference source, 3C 454.3, and two secondary reference sources, B2250+194 and B2252+172, for the guide star for the NASA/Stanford relativity mission *Gravity Probe B* (*GP-B*). For one epoch in 2004 May, we also obtained images at 5.0 and 15.4 GHz. The 35 8.4 GHz images for quasar 3C 454.3 confirm a complex, evolving, core-jet structure. We identified at each epoch a component, C1, near the easternmost edge of the core region. Simulations of the core region showed that C1 is located, on average, 0.18 ± 0.06 mas west of the unresolved "core" identified in 43 GHz images. We also identified in 3C 454.3 at 8.4 GHz several additional components that moved away from C1 with proper motions ranging in magnitude between $0.9\,c$ and $5\,c$. The detailed motions of the components exhibit two distinct bends in the jet axis located ~3 and ~5.5 mas west of C1. The spectra between 5.0 and 15.4 GHz for the "moving" components are steeper than those for C1. The 8.4 GHz images of B2250+194 and B2252+172, in contrast to those of 3C 454.3, reveal compact structures. The spectrum between 5.0 and 15.4 GHz for B2250+194 is inverted while that for B2252+172 is flat. Based on its position near the easternmost edge of the 8.4 GHz radio structure, close spatial association with the 43 GHz core, and relatively flat spectrum, we believe 3C 454.3 component C1 to be the best choice for the ultimate reference point for the *GP-B* guide star. The compact structures and inverted-to-flat spectra of B2250+194 and B2252+172 make these objects valuable secondary reference sources.

Key words: galaxies: active – galaxies: individual (B2252+172) – galaxies: jets – quasars: individual (3C 454.3, B2250+194) – radio continuum: galaxies – techniques: interferometric

1. INTRODUCTION

Gravity Probe B (*GP-B*) is the spaceborne relativity experiment developed by NASA and Stanford University to test two predictions of general relativity (GR). The experiment used four superconducting gyroscopes, contained in a low-altitude, polar orbiting spacecraft, to measure the geodetic effect and the much smaller frame-dragging effect. According to GR, each of these effects induces precessions of the gyroscopes. The predicted precession is 6.6 arcsec yr^{-1} for the geodetic effect and 39 mas yr^{-1} for the frame-dragging effect. *GP-B* was designed to measure the precessions with a standard error <0.5 mas yr^{-1} relative to distant inertial space. This space may be closely linked to the extragalactic International Celestial Reference Frame (ICRF), which is based on radio very long baseline interferometry (VLBI) measurements (Ma et al. 1998; Fey et al. 2004). Because of technical limitations, the spacecraft could not measure the precessions relative to such a frame directly, but rather only to an optically bright star. The proper motion of this chosen "guide star," IM Pegasi (=HR 8703; HD 216489; FK5 3829), was independently determined using VLBI measurements made relative to a fiducial point in the quasar 3C 454.3 (=4C 15.76; QSO J2253+1608). Two other radio sources, B2250+194 and B2252+172, are used as secondary reference sources to set a limit on the stability of the fiducial point. The radio structures of these three reference sources and their possible temporal changes are the subject of this paper. It is one of a series of seven papers reporting on the astronomical support for *GP-B*. For an overview of the paper series see Paper I (Shapiro et al. 2012).

The quasar 3C 454.3 ($z = 0.859$; Schmidt 1968) is an optically violent variable, and one of the brightest extragalactic radio sources (see, e.g., Stickel et al. 1994). Its milliarcsecond-scale structure has been extensively studied with VLBI. At radio frequencies between 1.7 GHz and 15 GHz, the structure of 3C 454.3 consists of a bright, relatively compact (unresolved) core region and an extended one-sided jet which is directed west-southwest near the core region and bends to the northwest ~5 mas from the core region (Pauliny-Toth et al. 1987; Bondi et al. 1996; Cawthorne & Gabuzda 1996; Kellermann et al. 1998; Pauliny-Toth 1998; Chen et al. 2005; Lister et al. 2009). The ~5 yr VLBI observing program of Pauliny-Toth et al. (1987) at 10.7 GHz traced the motions of four compact components that emerged from the core region and moved at superluminal apparent speeds in the range $5–9\,c$ along the curved path of the jet.[6] The results at 5 and 8.4 GHz by Pauliny-Toth (1998) give for one particular component a mean motion between 1983 and 1991 of $\sim 17\,c$. At frequencies of 22 and 43 GHz, the core region itself is resolved into two principal components oriented approximately east–west and separated

[4] Now at Okanagan College, 583 Duncan Avenue West, Penticton, BC, V2A 2K8, Canada and also at the National Research Council of Canada, Herzberg Institute of Astrophysics, Dominion Radio Astrophysical Observatory, PO Box 248, Penticton, BC, V2A 6K3, Canada.
[5] Now also at Hartebeesthoek Radio Astronomy Observatory, PO Box 443, Krugersdorp 1740, South Africa.

[6] Throughout this paper we assume a Hubble constant of $H_0 = 70\,\mathrm{km\,s^{-1}\,Mpc^{-1}}$ and a Friedmann–Robertson–Walker cosmology with $\Omega_M = 0.27$ and $\Omega_\Lambda = 0.73$.

by ∼0.6 mas (Kemball et al. 1996; Marscher 1998; Gómez et al. 1999; Jorstad et al. 2001; Chen et al. 2005; Jorstad et al. 2005). Moreover, observations at 43 GHz reveal that new components are occasionally ejected from the easternmost core-region component and move toward the westernmost core-region component with superluminal speeds anywhere in the range 3–13 c (Jorstad et al. 2001, 2005). The easternmost component is very compact at 43 GHz (<0.1 mas FWHM) and at that frequency is considered to be the "core," though its stationarity with respect to a celestial reference frame (e.g., the ICRF) has not been determined. The stationarity of a spatially related component at 8.4 GHz has recently been determined relative to an updated celestial reference frame (CRF), defined by ∼4000 compact extragalactic radio sources (see Paper III; Bartel et al. 2012).

The radio structure of quasar B2250+194 ($z = 0.284$; Snellen et al. 2002) is not nearly so well studied as that of 3C 454.3. In fact, only a handful of VLBI images of B2250+194 have been produced by others, and mostly as part of the U.S. Naval Observatory's astrometry program and the Very Long Baseline Array's (VLBA's) calibrator survey (Beasley et al. 2002). These images show that the source is only partially resolved at both 2.3 and 8.4 GHz on intercontinental baselines.

The radio source B2252+172 is catalogued in the National Radio Astronomy Observatory Very Large Array Sky Survey (NVSS; Condon et al. 1998), but has not previously been studied with VLBI. A spectrum for its optical counterpart has not yet been obtained, so its distance is not yet known.

In Section 2, we briefly summarize the process of selecting the extragalactic reference sources for our astrometry of the *GP-B* guide star. In Section 3, we describe our 35 sessions of VLBI observations, made between 1997 January and 2005 July. In Section 4, we describe our data reduction and analysis procedures. In Section 5, we show the 35 images made for quasar 3C 454.3 at 8.4 GHz, use model fitting to investigate the relative motions of the observed 8.4 GHz components, and present images made from VLBI observations at 5.0 and 15.4 GHz obtained on 2004 May 18. In Section 6, we show the 35 images made for quasar B2250+194 at 8.4 GHz, study its radio structure via model fitting, and present images made from VLBI observations at 5.0 and 15.4 GHz on 2004 May 18. In Section 7, we show the 12 images made for radio source B2252+172 at 8.4 GHz (which we observed starting only in 2002 November), investigate its radio structure via model fitting, and show the images made from the 5.0 and 15.4 GHz VLBI observations on 2004 May 18. We discuss our results in Section 8 and give our conclusions in Section 9.

2. THE SELECTION OF EXTRAGALACTIC REFERENCE SOURCES FOR THE *GP-B* GUIDE STAR

The principal astrometric requirements for our VLBI reference sources are that they be (1) radio bright and compact, (2) in close proximity on the sky to IM Peg, and (3) extragalactic in origin, with a core or other structural reference point stationary on the sky to a very high degree. These requirements are consistent with those of targeted astrometric VLBI experiments employing phase referencing (see, e.g., Lestrade et al. 1990). To summarize briefly, phase referencing requires that the reference source be detected in scans ∼1 minute or less in length, so that the interferometric phase delay, which changes with time, often very rapidly, can be successfully interpolated to scans of the target source. For this reason, the phase reference source must have a correlated flux density $\gtrsim$100 mJy, i.e., a flux density

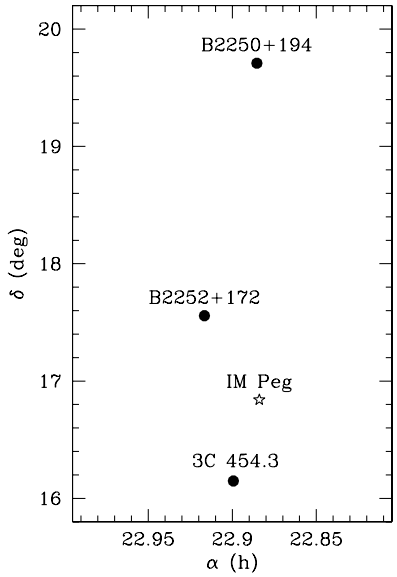

Figure 1. Positions (J2000) on the sky of the guide star, IM Peg, and the three reference sources. The linear scales are the same for α and δ. Here and in all images, north is up and east is to the left.

of at least this magnitude arising from a sufficiently compact emission region. Similarly, since the phase delay can change significantly with pointing direction, due mainly to radio propagation through the troposphere and ionosphere, the reference source should be located within ∼1° of the target source. Finally, if the morphology of the reference source is variable between observing sessions, then a point must be identified within the source image at every session that may confidently be assumed to be a (nearly) stationary feature of the source over the time spanned by our observing program.

The quasar 3C 454.3 is the only radio source that has both a correlated flux density >100 mJy and a relatively compact, milliarcsecond-scale structure within 1° of IM Peg (see Figure 1). Furthermore, 3C 454.3 was used as the only reference source for IM Peg in the phase-referenced mapping VLBI observations made for the *Hipparcos* frame-tie project from 1991 to 1994 (see Lestrade et al. 1999). Our continued observation of 3C 454.3 therefore provides a long time baseline for the guide star's proper-motion measurement. However, 3C 454.3 is a classic superluminal source with, in general, moving jet components. Without the benefit of a detailed and evolving model of its radio structure, the position accuracy of 3C 454.3 is limited (in the ICRF of Ma et al. 1998) to ∼1.5 mas, which is not quite sufficient to yield proper motions to within the ∼0.1 mas yr^{-1} standard error desired for *GP-B*. However, since our astrometric VLBI observations were designed so that we could produce high-quality images of our reference sources, we can identify a point in 3C 454.3 that is stationary on the sky to a much higher degree. All things considered, 3C 454.3 was the best choice to be our phase reference and main astrometric reference source.

The quasar B2250+194 is the next closest radio source on the sky to IM Peg that has a flux density >100 mJy and is compact on milliarcsecond scales. Indeed, B2250+194 has a more compact structure and displays more limited structural changes than 3C 454.3, as evidenced by the accuracy to which its position is measured in the ICRF (∼0.3 mas; see Fey et al. 2004). However, at a separation on the sky from IM Peg of 2.°9 (see Figure 1), its use as the primary astrometric reference could have introduced

large errors in the stellar proper-motion measurement (see, e.g., Pradel et al. 2006). Consequently, on the basis of its compact structure and "reasonably" small sky separation from IM Peg, we selected B2250+194 to be a secondary reference source.

The radio source B2252+172 is very compact and favorably located within ∼2° of, and approximately along the same north–south axis as, 3C 454.3, B2250+194, and IM Peg (see Figure 1). B2252+172 is relatively weak (∼20 mJy at 8.4 GHz), and was discovered only recently by the NVSS. In light of its low centimetric spectral index, we assume that B2252+172 is also extragalactic, even though its $R = 24$ optical counterpart is so faint that no spectrum has yet been obtained for it. We selected B2252+172 to serve as an additional reference source and astrometric check source, since its north–south alignment with 3C 454.3, B2250+194, and IM Peg helps to better model propagation-medium effects.

3. VLBI OBSERVATIONS

We carried out 35 sessions of 8.4 GHz ($\lambda = 3.6$ cm) VLBI observations of the *GP-B* guide star IM Peg between 1997 January and 2005 July using a global VLBI array of between 12 and 16 telescopes (see below). The considerations governing the scheduling of the observing sessions are outlined in Paper V (Ratner et al. 2012). For each session, we interleaved observations (scans) of IM Peg with those of our reference sources so that we could employ the phase-referencing technique (e.g., Shapiro et al. 1979; Bartel et al. 1986; Lestrade et al. 1990; Beasley & Conway 1995) to determine an accurate astrometric position for IM Peg. The phase reference source for all sessions was 3C 454.3. B2250+194 was also observed during all sessions. B2252+172 was included for the final 12 sessions, starting in 2002 November. We give the sky coordinates for each reference source in Paper III.

Our global VLBI array for each set of observations included the ten 25 m VLBA telescopes and, for increased sensitivity to the relatively weak IM Peg (flux density 0.2–80 mJy; see Paper V), two or more of the following large-aperture telescopes: the phased Very Large Array (VLA), the 100 m Effelsberg telescope, the 43 m Green Bank telescope, the 46 m Algonquin Radio Observatory telescope, and the three 70 m NASA-JPL Deep Space Network (DSN) telescopes. The total observing time after data editing and calibration for each session was 11–15 hr. During each session, we switched between IM Peg and each of the reference sources with a cycle time of between 5.5 and 7.3 minutes, in which IM Peg was observed for a minimum of 120 s, 3C 454.3 and B2250+194 for approximately 60 s each, and B2252+172 (when included) for approximately 75 s. The data were recorded with either the VLBA or Mark III system with sampling rates of 112, 128, or 256 Mbits s^{-1}, and were correlated with the National Radio Astronomy Observatory (NRAO) VLBA processor in Socorro, NM. At most epochs, both right-hand and left-hand circular polarizations were recorded. The specific characteristics of each set of observations are given in Table 1.

For our session on 2004 May 18, we observed IM Peg and the three reference sources at 5.0 GHz ($\lambda = 6.0$ cm) and 15.4 GHz ($\lambda = 2.0$ cm) in addition to using our standard frequency of 8.4 GHz. We observed for ∼2 hr at 8.4 GHz at the start of the observations, alternated ∼40 minute observing cycles at each of the three frequencies for the next ∼8 hr, observed at 8.4 GHz again for an extended period of ∼4 hr, and returned to the ∼40 minute cycle of three frequencies for the remaining ∼2 hr.

We used the VLA as a stand-alone interferometer (in addition to using it as an element of our VLBI array) for most of our sessions in order to monitor the variability of the total flux density and total circular polarization of IM Peg over the course of the 11–15 hr observing sessions. To set the flux-density scale for each set of VLA observations, we used one or both of the flux-density calibrator sources 3C 286 and 3C 48, with flux densities defined on the scale of Baars et al. (1977). We assume a standard error of ∼5% in the VLA-determined flux densities at each session. The range of values for the total flux density of IM Peg for each session, as well as the radio light curves in total intensity and total fractional circular polarization for a selected sample of sessions, are presented in Paper VII (Bietenholz et al. 2012). The flux densities[7] of reference sources 3C 454.3, B2250+194, and B2252+172 for each session are given in Table 2.

4. VLBI DATA REDUCTION AND ANALYSIS

We carried out the reduction and analysis of the VLBI data for the three reference sources with NRAO's Astronomical Image Processing System (AIPS). We performed the preliminary steps in the data reduction for each session, i.e., initial amplitude calibration (using system-temperature measurements and antenna gain curves), intermediate-frequency-channel bandpass and phase-offset correction, and data editing, in the usual manner (e.g., Walker 1999). We describe the remaining data reduction and analysis steps in some detail below.

For each of the stronger sources, 3C 454.3 and B2250+194, we fringe-fit and then iteratively self-calibrated (e.g., Cornwell & Fomalont 1999) and imaged the data. For fringe-fitting, we found a model consisting of a single point source to be adequate for determining the phase-delay rates and group delays for all telescopes (relative to a reference telescope) for both 3C 454.3 and B2250+194. For phase self-calibration, we found a starting model consisting of a single point source to be adequate for B2250+194 at all epochs, but inadequate for 3C 454.3 at most epochs.[8] For 3C 454.3, we used, instead, a starting model consisting of two point sources, which more accurately reflects the internal structure of the bright core region of the source (see Section 5). (We estimated the flux densities and relative positions of the two point sources by first fitting the model to the post-fringe-fit u–v data.) After self-calibrating in phase, we self-calibrated the data for each of 3C 454.3 and B2250+194 in amplitude. We stopped the iterative process when we achieved convergence in both the phase and amplitude self-calibrations. All images of 3C 454.3 and B2250+194 were generated using the CLEAN deconvolution algorithm (see Clark 1980) and the robust data-weighting scheme (Briggs 1995).

For our weakest reference source, B2252+172, our fringe-fitting for each session failed to find a reliable rate and delay

[7] B2250+194 and B2252+172 are unresolved by the VLA in all configurations, and we take as the total flux density of each source the peak flux density in the VLA interferometric image. In contrast, 3C 454.3 has an arcsecond-scale jet that is resolved by the VLA in the A, B, and C configurations. For observations made in these more extended configurations, we take as the flux density of 3C 454.3 the peak flux density of the core component in the VLA interferometric image. In the D configuration, we take as the flux density of 3C 454.3 the peak flux density in the VLA interferometric image, which includes contributions from both the variable core component and the ∼0.2 mJy arcsecond-scale jet.

[8] We judged the adequacy of the starting model by noting the number of iterations of phase self-calibration required to achieve convergence in the phase gains. At some epochs, a single-point-source starting model for 3C 454.3 would require several tens of iterations for convergence, whereas a two-point-source starting model would always require less than 10.

Table 1
8.4 GHz VLBI Observations of the *GP-B* Guide Star and Reference Sources

Start Date	Telescope[a]																	Total Time[b] (hr)	Cycle Time (minutes)	Recording Mode[c]	Circ. Pol.[d]
	Br	Fd	Hn	Kp	La	Mk	Nl	Ov	Pt	Sc	Y	Aq	Eb	Gb	Go	Ro	Ti				
1997 Jan 16	X	X	X	X	X	X	X	X	X	X	X	X	X		X	X		14.2	7.1	III-A	R
1997 Jan 18	X	X	X	X	X	X	X	X	X	X	X	X	X	X	X	X		14.2	7.1	III-A	R
1997 Nov 29	X	X	X	X	X	X	X	X	X	X	X				X	X		11.7	5.5	128-4-1	R,L
1997 Dec 21	X	X	X	X	X	X	X	X	X	X	X				X	X		14.8	5.5	128-4-1	R,L
1997 Dec 27	X	X	X	X	X	X	X	X	X	X	X				X	X		12.5	5.5	128-4-1	R,L
1998 Mar 1	X	X	X	X	X	X	X	X	X	X	X				X	X	X	14.9	5.5	128-4-1	R,L
1998 Jul 12	X	X	X	X	X	X	X	X	X	X	X				X	X	X	15.1	5.5	128-4-1	R,L
1998 Aug 8	X	X	X	X	X	X	X	X	X	X	X		X		X	X	X	15.1	5.5	128-4-1	R,L
1998 Sep 16	X	X	X	X	X	X	X	X	X	X	X		X		X	X	X	15.1	5.5	128-4-1	R,L
1999 Mar 13	X	X	X	X	X	X	X	X	X	X	X		X		X	X		15.1	5.5	128-4-1	R,L
1999 May 15	X	X	X	X	X	X	X	X	X	X	X		X		X	X	X	15.1	5.5	128-4-1	R,L
1999 Sep 18	X	X	X	X	X	X	X	X	X	X	X		X		X		X	15.2	5.5	128-4-1	R,L
1999 Dec 9	X	X	X	X	X	X	X	X	X	X	X		X		X	X		14.5	5.5	128-4-1	R,L
2000 May 15	X	X	X	X		X	X	X	X	X	X		X			X	X	14.6	5.5	128-4-1	R,L
2000 Aug 7	X	X	X	X	X	X	X	X	X	X	X		X		X	X		15.1	5.5	128-4-1	R,L
2000 Nov 5	X	X	X	X	X	X	X	X	X	X	X		X		X	X	X	15.1	5.5	128-4-1	R,L
2000 Nov 6	X	X	X	X	X	X	X	X	X	X	X				X			13.3	5.5	128-4-1	R,L
2001 Mar 31	X	X		X	X	X	X	X	X	X	X		X		X	X	X	15.2	5.5	128-4-1	R,L
2001 Jun 29	X	X	X	X	X	X	X	X	X	X	X				X	X	X	13.9	5.5	128-4-1	R,L
2001 Oct 19	X	X	X	X	X	X	X	X	X	X	X		X		X	X	X	14.9	5.5	128-4-1	R,L
2001 Dec 21	X	X	X	X	X	X	X	X	X	X			X		X		X	15.1	5.5	128-4-1	R,L
2002 Apr 14	X	X	X	X	X	X	X		X		X		X		X	X	X	13.9	5.5	128-4-1	R,L
2002 Jul 14	X	X	X	X	X	X	X	X	X	X			X		X	X	X	14.8	5.5	128-4-1	R,L
2002 Nov 20	X	X	X	X	X	X	X	X	X	X					X	X		10.8	7.3	128-4-1	R,L
2003 Jan 26	X	X	X	X	X	X	X	X	X	X	X		X		X	X		14.2	7.3	128-4-1	R,L
2003 May 18	X	X	X	X	X	X	X	X	X	X	X		X		X	X	X	15.2	7.3	128-4-1	R,L
2003 Sep 8	X	X	X	X	X	X	X	X	X	X	X		X		X	X	X	15.1	7.3	128-4-1	R,L
2003 Dec 5	X	X	X	X	X	X	X	X	X	X			X		X	X	X	15.2	11.0[e]	128-4-1	R,L
2004 Mar 6	X	X	X	X	X	X	X	X	X	X	X		X		X	X	X	15.2	11.0	128-4-1	R,L
2004 May 18	X	X	X	X	X	X	X	X		X	X		X		X	X	X	15.2	11.0	128-4-1	R,L
2004 Jun 26	X	X	X	X	X	X	X	X	X	X	X				X	X	X	15.2	11.0	128-4-1	R,L
2004 Dec 11	X	X	X	X	X	X	X	X	X	X	X		X			X	X	15.1	11.0	128-4-1	R,L
2005 Jan 15	X	X	X	X	X	X	X	X	X	X	X		X		X	X	X	13.4	11.0	256-4-2	R,L
2005 May 28	X		X	X	X	X	X	X	X	X	X		X		X	X	X	13.3	11.0	256-4-2	R,L
2005 Jul 16	X	X	X	X	X	X	X	X	X	X	X		X		X	X	X	13.3	11.0	256-4-2	R,L

Notes.

[a] Br = 25 m, NRAO, Brewster, WA, USA; Fd = 25 m, NRAO, Fort Davis, TX, USA; Hn = 25 m, NRAO, Hancock, NH, USA; Kp = 25 m, NRAO, Kitt Peak, AZ, USA; La = 25 m, NRAO, Los Alamos, NM, USA; Mk = 25 m, NRAO, Mauna Kea, HI, USA; Nl = 25 m, NRAO, North Liberty, IA, USA; Ov = 25 m, NRAO, Owens Valley, CA, USA; Pt = 25 m, NRAO, Pie Town, NM, USA; Sc = 25 m, NRAO, St. Croix, Virgin Islands, USA; Y = phased VLA equivalent diameter 130 m, NRAO, near Socorro, NM, USA; Aq = 46 m, ISTS (now CRESTech/York U.), Algonquin Park, ON, Canada; Eb = 100 m, MPIfR, Effelsberg, Germany; Gb = 43 m, NRAO, Green Bank, WV, USA; Go = 70 m, NASA-JPL, Goldstone, CA, USA; Ro = 70 m, NASA-JPL, Robledo, Spain; Ti = 70 m, NASA-JPL, Tidbinbilla, Australia.

[b] Session duration (including telescope slew time) after data editing.

[c] Recording mode: III-A = Mk III mode A, 56 MHz recorded; 128-4-1 = VLBA format, 128 Mbps recorded in four baseband channels with 1 bit sampling; 256-4-2 = VLBA format, 256 Mbps recorded in four baseband channels with 2 bit sampling.

[d] The sense of circular polarization recorded: R = right and L = left circular polarization (IEEE convention).

[e] For the last eight sessions, we employed an 11.0 minute major cycle consisting of two minor cycles, one 6.3 minutes in length and including all four sources (3C 454.3, IM Peg, B2250+194, and B2252+172) and one 4.7 minutes in length and including all sources except 2252+172.

solution (with signal-to-noise ratio, S/N $\geqslant$ 5) on 10%–50% of scans for at least one, and usually several, telescopes (relative to a reference telescope). Instead we used the final image of 3C 454.3 to estimate the phase component of the complex antenna gains at the position of B2252+172 as a function of time (see Section 4.1), and the images of both 3C 454.3 and B2250+194 to estimate the amplitude component as a function of time. (Note that, in contrast to the phase gains, the amplitude gains are largely unaffected by inaccuracies in the propagation-medium model.) For each telescope, the amplitude gains for sources 3C 454.3 and B2250+194 were identical to within 2%, so we smoothed them together over intervals of 30 minutes to 1 hr before using them to fine-tune the amplitude calibration for B2252+172.

4.1. Phase-referenced Imaging of B2252+172

At each session, the phase components of the complex antenna gains were derived for every scan of 3C 454.3, with a cadence of 5.5–7.3 minutes, and interpolated to the effective time of the B2252+172 scans. We found that phase connection between successive scans of 3C 454.3 was not possible in some instances for time ranges in which at least one telescope on a baseline was viewing the source at an elevation $\lesssim$20°. Any time range of data for which phase connection on a given baseline

Table 2
Flux Densities[a] of 3C 454.3, B2250+194, and B2252+172

Start Date	3C 454.3[b] (Jy)	B2250+194 (mJy)	B2252+172 (mJy)
1997 Jan 16	12.16 ± 0.65	438 ± 22	
1997 Jan 18	12.06 ± 0.64	430 ± 21	
1997 Nov 29	11.31 ± 0.57(D)	469 ± 24	
1997 Dec 21	10.54 ± 0.54(D)	451 ± 23	
1997 Dec 27	10.01 ± 0.51(D)	432 ± 22	
1998 Mar 1	10.84 ± 0.56	488 ± 24	
1998 Jul 12	11.80 ± 0.60	447 ± 22	
1998 Aug 8	11.49 ± 0.61	417 ± 24	
1998 Sep 16	11.46 ± 0.61	455 ± 23	
1999 Mar 13	11.16 ± 0.58(D)	432 ± 23	
1999 May 15	11.09 ± 0.57(D)	455 ± 23	
1999 Sep 18	12.05 ± 0.74	418 ± 21	
1999 Dec 9	10.74 ± 0.55	468 ± 23	
2000 May 15	9.86 ± 0.52	433 ± 22	
2000 Aug 7	9.13 ± 0.47(D)	420 ± 21	
2000 Nov 5	9.14 ± 0.46	436 ± 22	
2000 Nov 6	9.12 ± 0.46	441 ± 22	
2001 Mar 31	11.17 ± 0.59	443 ± 24	
2001 Jun 29	10.92 ± 0.56	395 ± 20	
2001 Oct 19	9.70 ± 0.49(D)	380 ± 19	
2001 Dec 21(*)	9.25 ± 0.93	406 ± 41	
2002 Apr 14	9.30 ± 0.47	359 ± 18	
2002 Jul 14(*)	9.32 ± 0.93	354 ± 35	
2002 Nov 20(*)	9.47 ± 0.95	396 ± 40	18.0 ± 1.9
2003 Jan 26	10.80 ± 0.54	421 ± 21	25.0 ± 1.3
2003 May 18	10.42 ± 0.54	428 ± 22	27.0 ± 1.4
2003 Sep 8	9.66 ± 0.48	480 ± 24	21.6 ± 1.1
2003 Dec 5(*)	9.31 ± 0.93	488 ± 49	19.1 ± 1.9
2004 Mar 6	8.99 ± 0.45	512 ± 26	17.2 ± 0.9
2004 May 18	8.58 ± 0.43	533 ± 27	16.0 ± 0.8
2004 May 18(C)[c]	10.45 ± 0.53	381 ± 19	17.3 ± 0.9
2004 May 18(U)[c]	5.94 ± 0.42	561 ± 39	11.5 ± 0.8
2004 Jun 26	8.59 ± 0.43(D)	525 ± 26	15.9 ± 0.8
2004 Dec 11	9.36 ± 0.47	507 ± 26	18.3 ± 0.9
2005 Jan 15	9.58 ± 0.48	531 ± 27	17.5 ± 0.9
2005 May 28	9.41 ± 0.47	498 ± 25	23.0 ± 1.2
2005 Jul 16	9.56 ± 0.48	519 ± 25	26.5 ± 1.3

Notes.
[a] For all but four epochs (marked with "*"), the tabulated value for the flux density is that estimated with the VLA Stokes-*I* data. For the remaining epochs, the (Stokes-*I*) flux density was estimated from the VLBI data. The standard error is the root-sum-square (rss) of the statistical standard error found in estimating the flux density and a 5% (10% for VLBI) systematic error allowed for calibration of the flux-density scale (see Section 4).
[b] Epochs marked with a "D" indicate that the VLA was in its D configuration. The nominal value for the flux density of 3C 454.3 for these epochs includes a ∼0.2 mJy contribution from the arcsecond-scale jet.
[c] C indicates 5.0 GHz; U indicates 15.4 GHz; all other observations were at 8.4 GHz.

was problematic was flagged but not deleted. We Fourier-inverted the unflagged B2252+172 data and used the CLEAN deconvolution algorithm to produce a phase-referenced image of the source. Using the phase-referenced image as a starting model, we then phase-self-calibrated the full set of B2252+172 data at each session (including the data previously flagged) over time intervals from scan lengths to ∼20 minutes, depending on the flux density of the source. The quality of the image (judged by the ratio of peak brightness to root-mean-square, "rms," background and the ratio of peak to minimum brightness) produced after a few iterations of phase self-calibration was, for each session, significantly higher ($\gtrsim$50% improvement in each ratio) than that of the strictly phase-referenced image. We also self-calibrated the B2252+172 data at each session in amplitude, but found little improvement ($\lesssim$5% improvement in each ratio) in the resulting image over the image produced in the phase-only self-calibration process. The final images for B2252+172 were produced with data that were phase-self-calibrated only. As for 3C 454.3 and B2250+194, all images of B2252+172 were generated using the CLEAN deconvolution algorithm and the robust data-weighting scheme.

4.2. Model Fitting

To derive quantitative results for each of the three reference sources, we also fit simple brightness-distribution models to either the image plane data using the AIPS program JMFIT, or the *u*–*v* plane data using the AIPS program OMFIT. Both programs utilize weighted least-squares algorithms. In the case of the *u*–*v* plane model fits, we first averaged the data within each individual scan. We describe the model used in each fit, and the process of estimating the standard errors in the fit parameters, source by source, in Sections 5, 6, and 7.

4.3. Standard Error in the VLBI Amplitude Calibration

The mean ratios of VLBI-determined to VLA-determined flux densities are 0.94 ± 0.04 for 3C 454.3 (see Table 3) and 0.97 ± 0.04 for B2250+194 (see Table 9). However, the ratios are systematically lower (and more variable) for epochs before 2003 January, compared with those after, likely due to improved accuracy and implementation of the system-temperature measurements and/or gain curves for the large-aperture telescopes. We estimate that our VLBI array "resolves out" only ∼4% of the total (VLA-determined) flux density for 3C 454.3 and ∼3% of the total flux density for B2250+194. In order to simplify our quantitative analysis, we adopt a conservative standard error of 10% for all VLBI-determined flux densities unless stated otherwise.

5. QUASAR 3C 454.3: THE MAIN REFERENCE SOURCE

5.1. VLBI Images at 8.4 GHz

In Figure 2 we present the 8.4 GHz images of 3C 454.3 generated from each of the 35 sessions of VLBI observations made between 1997 January and 2005 July. Each image is convolved with a Gaussian (CLEAN) restoring beam of size and shape determined, as usual, from a fit to the main lobe of the interferometer beam for that set of observations. The median size of the minor axis of the restoring beam is 0.67 mas (FWHM), and the median ratio of major to minor axis is 2.5. The image characteristics are summarized in Table 3. The images in the figure are aligned on the center of the easternmost component of the radio structure observed at each epoch (see Section 5.2). The coordinates in each image are relative to the phase center,[9] which is generally offset from the brightness peak by <0.02 mas in each of α and δ.

Each of our VLBI images of 3C 454.3 exhibits a radio structure generally consistent with that observed previously for this source at frequencies between 1.7 and 15 GHz, namely a bright, relatively compact core region and a bent milliarcsecond-scale

[9] The phase center (i.e., position [0, 0] in the image) refers to the assumed source position used at the correlator. During the phase-self-calibration process, the offset between the true and assumed positions, for a flux-density-averaged point in the radio structure, is removed from the *u*–*v* data.

Table 3
3C 454.3 Image Characteristics

Start Date	Peak ($\mathrm{Jy}\,\Omega_b^{-1}$) [1]	Min. ($\mathrm{mJy}\,\Omega_b^{-1}$) [2]	rms ($\mathrm{mJy}\,\Omega_b^{-1}$) [3]	Θ_{maj} (mas) [4]	Θ_{min} (mas) [5]	P.A. (°) [6]	CLEAN (Jy) [7]	$[\frac{\mathrm{CLEAN}}{\mathrm{VLA}}]$ [8]
1997 Jan 16	6.14	−4.87	0.76	1.68	0.72	−6.43	10.70	0.88
1997 Jan 18	6.05	−4.39	0.66	1.83	0.70	−8.43	10.61	0.88
1997 Nov 29	6.20	−5.87	0.80	1.77	0.93	−2.93	9.72	0.86
1997 Dec 21	6.23	−4.33	0.58	1.68	0.83	−4.08	10.15	0.96
1997 Dec 27	5.91	−3.88	0.72	1.75	0.80	−5.40	9.54	0.95
1998 Mar 1	6.00	−5.05	0.56	1.59	0.82	−3.80	9.58	0.88
1998 Jul 12	6.10	−5.93	0.71	1.75	0.64	−8.19	10.48	0.89
1998 Aug 8	6.27	−5.79	0.74	1.78	0.65	−8.36	11.04	0.96
1998 Sep 16	6.18	−5.77	0.73	1.80	0.69	−7.05	10.69	0.93
1999 Mar 13	5.40	−5.91	0.59	1.73	0.68	−7.90	9.62	0.86
1999 May 15	5.90	−4.39	0.55	1.66	0.62	−7.61	10.41	0.94
1999 Sep 18	8.16	−7.71	1.02	1.76	0.81	−9.28	12.32	1.02
1999 Dec 9	5.04	−5.18	0.52	1.73	0.67	−6.46	9.46	0.88
2000 May 15	3.37	−5.47	0.77	1.54	0.59	−6.66	9.30	0.94
2000 Aug 7	4.60	−3.09	0.38	1.87	0.74	−7.95	9.31	1.02
2000 Nov 5	4.14	−4.92	0.71	1.63	0.64	−7.20	8.77	0.96
2000 Nov 6	4.98	−5.18	0.69	1.79	0.99	−3.38	8.84	0.97
2001 Mar 31	5.13	−8.92	0.90	1.56	0.63	−7.18	9.65	0.86
2001 Jun 29	5.32	−5.10	0.54	1.78	0.75	−4.19	10.08	0.92
2001 Oct 19	3.78	−5.93	0.88	1.83	0.64	−8.35	9.35	0.96
2001 Dec 21	4.78	−3.53	0.51	1.71	0.89	−8.94	9.25	...
2002 Apr 14	3.97	−7.74	0.89	2.73	0.66	−13.04	8.67	0.93
2002 Jul 14	4.18	−3.88	0.41	1.71	0.63	−6.91	9.32	...
2002 Nov 20	4.90	−7.05	0.70	1.76	0.75	−0.90	9.47	...
2003 Jan 26	4.93	−5.02	0.70	1.81	0.70	−4.59	10.35	0.96
2003 May 18	3.54	−5.07	0.53	1.62	0.59	−7.27	9.80	0.94
2003 Sep 8	3.02	−4.32	0.63	1.67	0.60	−8.15	9.34	0.97
2003 Dec 5	2.90	−7.79	0.98	1.69	0.59	−9.52	9.31	...
2004 Mar 6	2.85	−7.48	0.97	1.62	0.60	−7.87	8.97	1.00
2004 May 18	2.73	−4.25	0.83	1.76	0.68	−8.64	8.41	0.98
2004 May 18(C)[a]	3.93	−10.6	1.81	3.03	0.99	−9.99	9.73	0.93
2004 May 18(U)[a]	1.13	−14.0	2.24	0.98	0.33	−8.58	5.82	0.98
2004 Jun 26	2.85	−3.63	0.45	1.61	0.76	−3.30	8.03	0.94
2004 Dec 11	2.78	−3.02	0.34	1.58	0.61	−8.16	8.94	0.96
2005 Jan 15	2.76	−2.77	0.41	1.64	0.61	−8.22	9.00	0.94
2005 May 28	2.68	−4.94	0.73	1.62	0.59	−7.80	9.17	0.98
2005 Jul 16	2.50	−1.89	0.23	1.66	0.62	−7.13	9.07	0.95

Notes. Columns 1 and 2: positive and negative extrema ($\Omega_b \equiv$ CLEAN restoring beam area); Column 3: rms background level ("far" away from source); Columns 4–6: CLEAN restoring beam major axis (FWHM), minor axis (FWHM), and position angle (east of north); Column 7: total CLEAN flux density; Column 8: ratio of VLBI-determined (Column 7) to VLA-determined (Table 2) flux density for all epochs at which the VLA observed. The estimated standard error in the VLBI-determined flux densities is 10%.
[a] C indicates 5.0 GHz; U indicates 15.4 GHz; all other observations were at 8.4 GHz.

jet. Nevertheless, a number of structural changes are apparent over the ∼8.5 yr period of our observing program. The most significant changes take place in the core and inner-jet regions. The core region, which we roughly define as the easternmost ∼1 mas of the source, is visibly extended mainly east–west, ranging in appearance from a single elongated emission region to a marginally resolved double-peaked emission region. We model the core region at each of our 35 epochs with two compact components separated by 0.45–0.7 mas (see Section 5.2.1). The two-component, or indeed multi-component, structure of the core and inner-jet regions of 3C 454.3 was first observed by Pauliny-Toth et al. (1987) during their ∼5 yr VLBI program at 10.7 GHz. Their images show that the two easternmost components have a relatively constant 0.5–0.6 mas separation, and that others move approximately westward away from them with superluminal apparent velocities. Our images likewise show that new components occasionally emerge to the west–southwest of the core region and move approximately westward toward the extended jet. We discuss the motions in the inner-jet region in Section 5.2.2. The brightness peak of the jet, located ∼5.5 mas west of the easternmost core-region component, also appears to move with respect to the core region, but at a lower apparent velocity, and northward rather than westward. Beyond this point, the axis of the jet bends sharply to the northwest. We discuss the motion of the jet peak, and extended jet as a whole beyond the peak, in Section 5.2.3.

To assign a systematic error to quantities estimated in our image-plane analysis in the next section, we also produced for each set of observations an image (not shown) of 3C 454.3 using a common restoring beam. We chose a beam with a major axis of 2.00 mas (FWHM), a minor axis of 0.80 mas (FWHM), and a position angle (P.A.) of 0° (east of north) to encompass the majority of the CLEAN restoring beams in the nominal-resolution images (see Table 3), and to reflect the median ratio

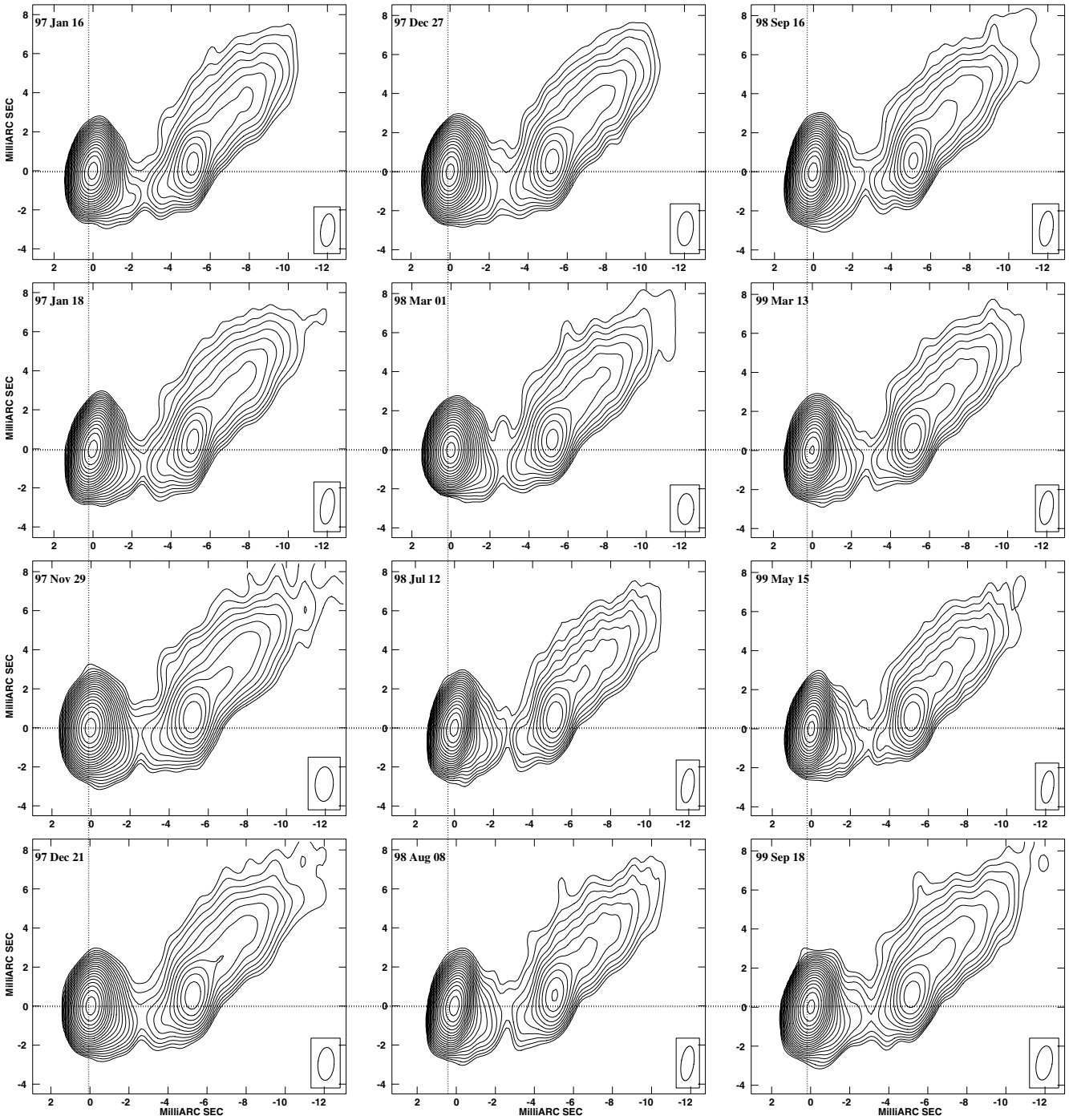

Figure 2. 8.4 GHz VLBI images of 3C 454.3 for each of our 35 observing sessions between 1997 January and 2005 July. Contour levels differ by factors of $\sqrt{2}$, starting in each image at 10 mJy beam^{-1}. Image characteristics are summarized in Table 3. The restoring beam is indicated in the bottom right-hand corner of each image. The images are aligned, as indicated by the dotted lines, on the center of the easternmost component, C1 (see Section 5.2.1).

of major to minor axes of the CLEAN restoring beams. For 28 epochs, the common restoring beam fully encompassed the CLEAN restoring beam, so we simply convolved the nominal-resolution image with the larger common restoring beam. For five of the seven remaining epochs, we first generated an image with a CLEAN restoring beam slightly smaller than the common restoring beam, by increasing the relative weights on the longer baselines during imaging, and then convolved the new image with the common restoring beam. For two epochs, namely 2000 November 6 and 2002 April 14, no choice of data weights produced a beam smaller than the common restoring beam, but we still forced the CLEAN restoring beam to have the dimensions and orientation of the common restoring beam (resulting in a mild super-resolution).

5.2. Image-plane Model Fitting at 8.4 GHz

We performed a detailed analysis of the changing 8.4 GHz radio structure of 3C 454.3 via model fitting in the image plane. For this analysis we used the nominal-resolution images shown in Figure 2. Fitting in the image plane facilitates dissection of

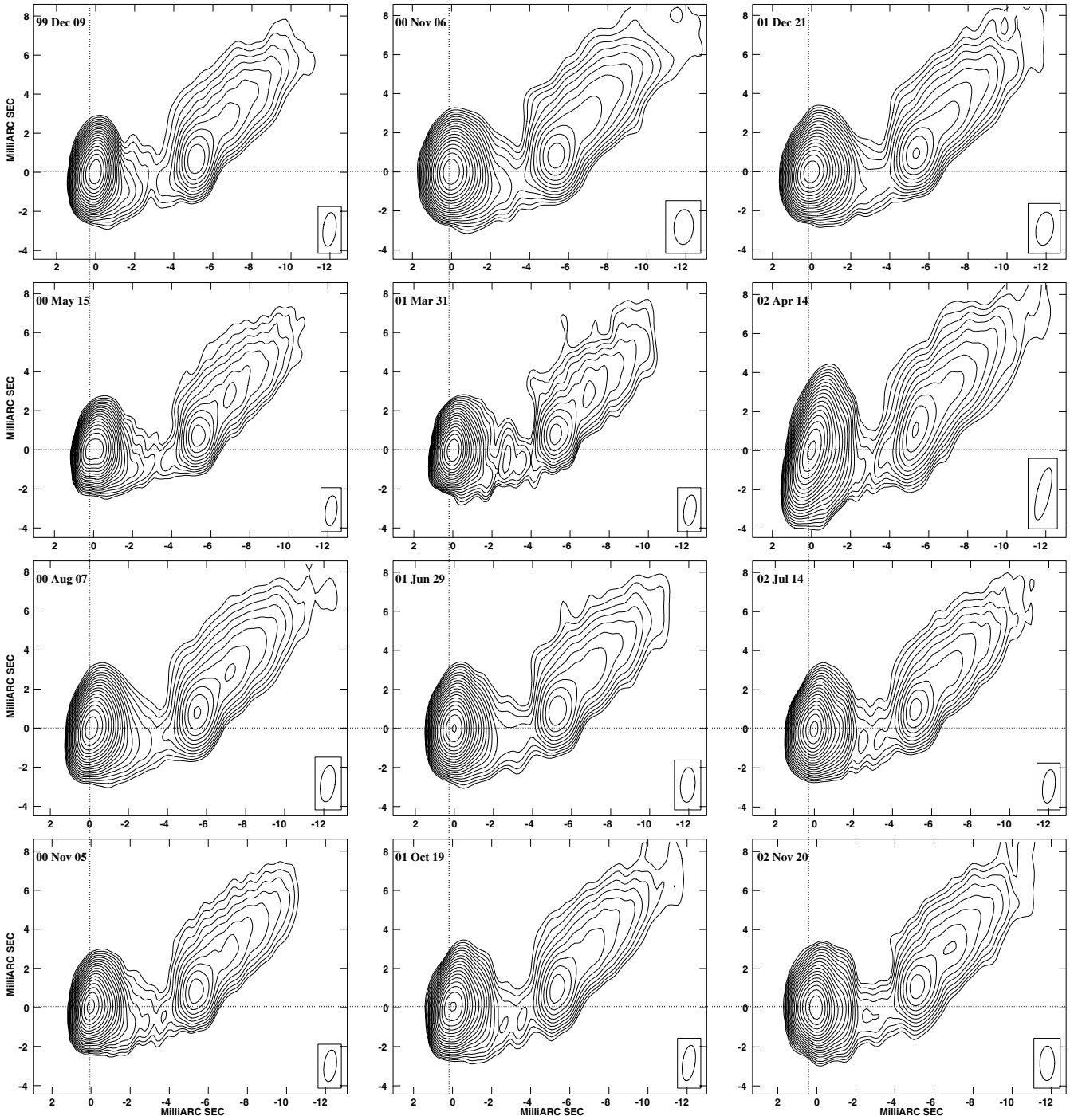

Figure 2. (Continued)

the complex radio structure over its full brightness range. In the $u-v$ plane (see Section 5.3), the bright core-region components dominate the low-surface-brightness jet components. In the image plane, we can isolate structure and, in turn, investigate the core and jet regions. However, concerns about systematic errors in the image-plane analysis such as from (CLEAN) deconvolution errors and the differing resolution at each epoch have to be investigated and quantified as best as possible. In the remainder of this section, we discuss the image-plane-based model fitting of the core, inner-jet, and extended-jet regions of 3C 454.3, using windows allocated approximately as shown in Figure 3. For ease of reference, we also indicate in Figure 3 the approximate positions of the model components discussed below.

5.2.1. Core Region

Several of our images of 3C 454.3, in particular those after 2003 January, show that the easternmost ∼1 mas of the 8.4 GHz radio structure is marginally resolved into two components oriented approximately east–west. We fit to the core region at each epoch a model consisting of two point sources, and, for comparison, a model consisting of a single elliptical Gaussian. The two-component model fit the image data for the core region better (yielding 30% to 70% lower values of the post-fit rms residuals) at all epochs, including those in which the core region appears only slightly elongated in Figure 2. The results of the two-component fit are given in Table 4. We refer to the

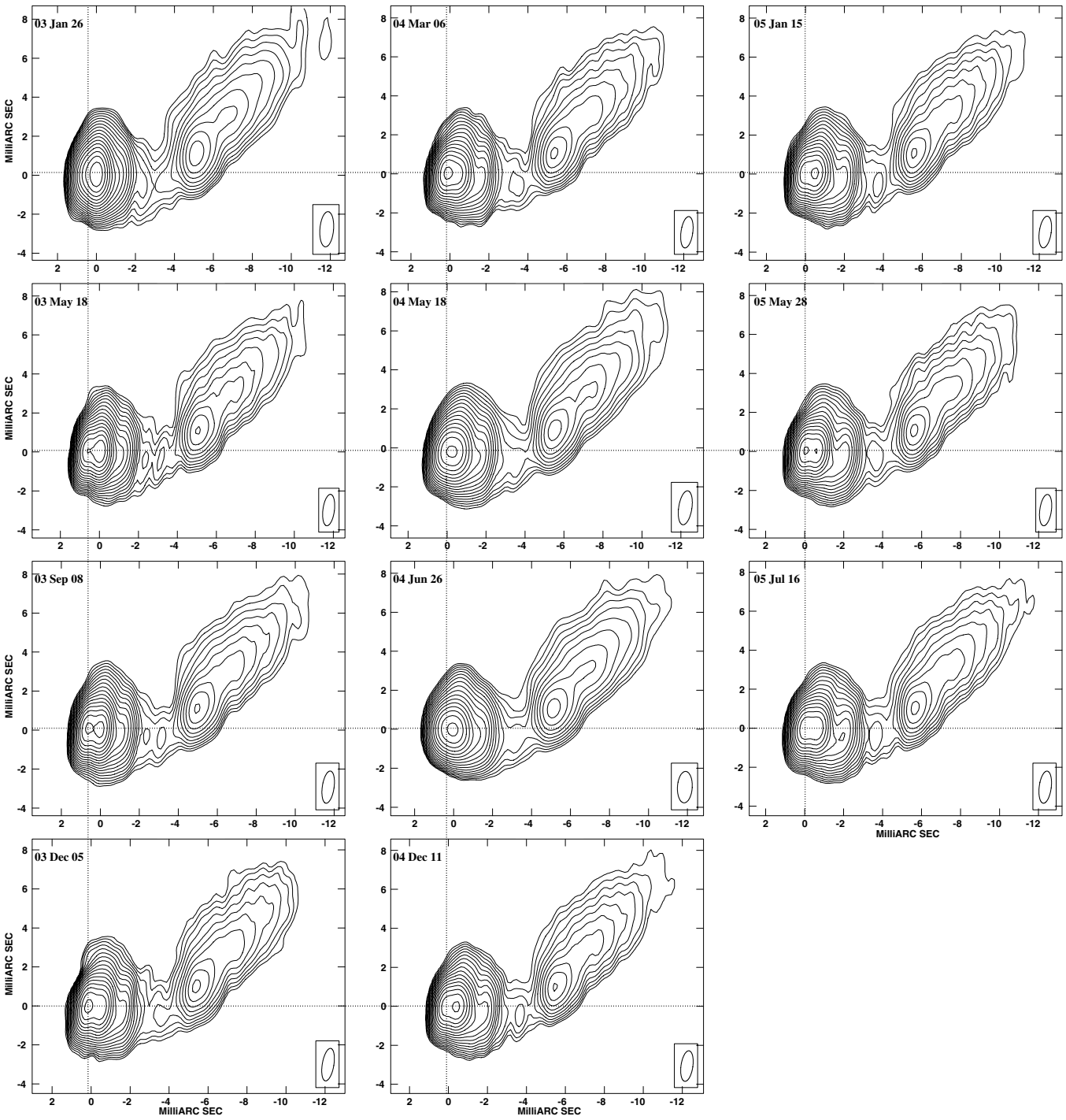

Figure 2. (Continued)

easternmost component as C1 and the westernmost component as C2. The tabulated standard errors in the flux densities and positions of C1 and C2 at each epoch include contributions, added in quadrature, from the statistical standard error of the fit and from the systematic errors associated with deconvolution (see Section 5.2.4) and the "choice" of image resolution. The last error is taken at each epoch to be the difference between the parameter estimate from the fit to the nominal-resolution image (Figure 2) and the corresponding parameter estimate from the fit to the common-resolution image. At every epoch, the systematic errors are ∼10–20 times larger than the statistical standard errors. Unless otherwise noted, the quoted errors for all model parameters are standard errors, which include the systematic error estimate.

In Figure 4, we plot at each epoch the separation of C2 from C1. We see that this separation increased by ∼0.25 mas over the ∼8.5 yr period of our observing program, largely in the α coordinate. We determined, via a weighted-least-squares fit of a straight line to the separation at all 35 epochs, a relative proper motion for C2 with respect to C1 of -0.034 ± 0.003 mas yr^{-1} in α and -0.014 ± 0.003 mas yr^{-1} in δ. (We use weighted least-squares for all proper-motion determinations.) The quoted uncertainties are the statistical standard errors of the fit, scaled by a common factor so that the χ^2 per degree of freedom is

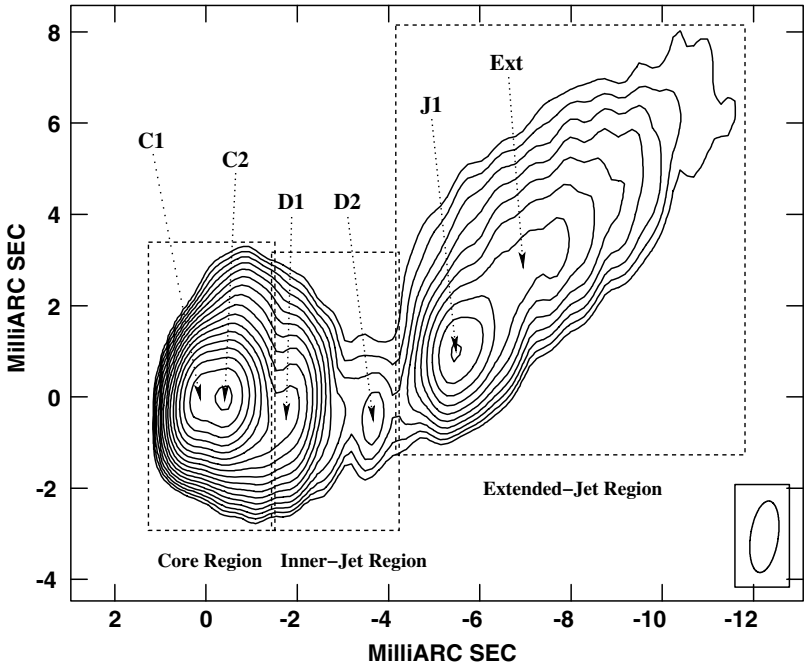

Figure 3. VLBI image of 3C 454.3 (2004 December 11) showing the approximate locations of the model components (labeled) and fitting windows (dashed rectangles). The restoring beam is at the lower right.

unity. We performed the same weighted fit to the separations determined for the common-resolution images, and found that the relative proper motion was 0.5σ larger in α and 0.2σ smaller in δ, where σ is the statistical standard error of the nominal (differing-resolution) case. Taking the difference as an estimate of the systematic error in the determination of the relative proper motion in the nominal case, and adding in quadrature the statistical standard error for the nominal case, we get a relative proper motion (nominal value and standard error) for C2 with respect to C1 of -0.034 ± 0.004 mas yr^{-1} in α and -0.014 ± 0.004 mas yr^{-1} in δ. (We compute the standard errors in the relative proper motions of components in the same way throughout Section 5.2.)

The two-component model described above obviously does not account for all the structure seen in, or very near, the core region at each epoch. In particular, the two-component model fails to accurately describe low-level emission extending west-southwest from C2 with surface brightness 5%–25% of the peak brightness. At many epochs, this emission appears to be associated with the emergence of a new component into the inner-jet region (see, e.g., Figure 3). Unfortunately, our resolution is not sufficient to adequately constrain a more elaborate model for the core region. In an attempt to simultaneously describe the bright components of the core region and what we call a transition component that moves between the core and inner-jet regions, we extended at each epoch the core-region fitting window ∼1 mas west into the inner-jet region and fit a model consisting of three point sources. For 13 epochs, the fit positions and flux densities of each of C1 and C2 in the three-component and two-component models differ by no more than two times the standard error in the two-component model (see Table 4). For these epochs, we (somewhat arbitrarily) consider the three-component model to give an acceptable description of the two core-region components and the transition component. The fit results for the transition component for these epochs and a brief description of the results for the remaining epochs are presented in Section 5.2.2. In addition to the extension due to the transition component, there also appears to be core-region emission north of C2, especially at our later epochs. This emission is at a very low level and likely does not affect the results from the two-component model for either C1 or C2.

How well does our simple two-component model represent the underlying structure of the core region of 3C 454.3? VLBI images at 43 GHz and 86 GHz reveal a great complexity and variability in the easternmost ∼1 mas of 3C 454.3. At the extreme east is a very compact component ($\lesssim$0.03 mas FWHM at 86 GHz; Krichbaum et al. 2006b), considered by various authors to be the VLBI "core." New components are occasionally ejected from approximately the position of this core and then move west-northwest (along p.a. $\approx -70°$) at superluminal apparent velocities in the range 3–13 c (Jorstad et al. 2001, 2005). At a distance of ∼0.65 mas from the core, the moving components are thought to encounter a bend or a recollimation shock in the jet (see Gómez et al. 1999) and brighten to produce at 43 GHz a component that is approximately stationary relative to the core at that frequency. The separation of the core and the "stationary" component at 43 GHz is similar to the separation of the two easternmost components observed at 10.7 GHz by Pauliny-Toth et al. (1987) and also to the mean separation of C1 and C2 in our 8.4 GHz images. Diffuse emission appears in the 43 GHz images to the north and northwest of the "stationary" component at various epochs, but the moving components emerge primarily to the west or southwest of the "stationary" component (e.g., Jorstad et al. 2005). The ejection from the core of new jet components, and the motions of these components toward and beyond the "stationary" component, may be responsible for the apparent "oscillations" we observe in the 8.4 GHz separation of C2 relative to C1 (see Figure 4). The proper motion of C2 relative to C1 could be a consequence of the westward motion of a particularly bright jet component through the position of the "stationary" component in the latter part of our observing period (see Section 8.1).

To better quantify the spatial relationship of component C1 in our 8.4 GHz images to the core as imaged at 43 GHz, and

Table 4
3C 454.3 Image Plane 8.4 GHz Model Parameters: Core Region

Start Date	Component C1						Component C2					
	$S_{8.4}$ (Jy) [1]	σ_S (Jy) [2]	$\Delta\alpha$ (mas) [3]	σ_α (mas) [4]	$\Delta\delta$ (mas) [5]	σ_δ (mas) [6]	$S_{8.4}$ (Jy) [7]	σ_S (Jy) [8]	$\Delta\alpha$ (mas) [9]	σ_α (mas) [10]	$\Delta\delta$ (mas) [11]	σ_δ (mas) [12]
1997 Jan 16	3.39	0.21	0.243	0.019	−0.044	0.013	3.41	0.18	−0.224	0.029	0.013	0.011
1997 Jan 18	3.41	0.25	0.239	0.026	−0.047	0.021	3.32	0.19	−0.225	0.039	0.008	0.014
1997 Nov 29	5.24	0.34	0.141	0.017	−0.004	0.010	2.15	0.16	−0.378	0.078	0.046	0.011
1997 Dec 21	5.04	0.56	0.082	0.041	0.004	0.017	2.61	0.39	−0.386	0.110	0.037	0.012
1997 Dec 27	4.79	0.44	0.126	0.029	0.000	0.016	2.45	0.29	−0.339	0.092	0.003	0.018
1998 Mar 1	4.19	0.49	0.172	0.035	0.000	0.010	3.07	0.36	−0.253	0.083	−0.007	0.010
1998 Jul 12	3.04	0.16	0.353	0.016	0.000	0.012	5.24	0.26	−0.117	0.017	−0.008	0.010
1998 Aug 8	3.30	0.18	0.445	0.015	0.002	0.010	5.44	0.27	−0.034	0.019	−0.014	0.010
1998 Sep 16	3.39	0.18	0.341	0.015	0.006	0.016	4.97	0.25	−0.133	0.017	−0.022	0.010
1999 Mar 13	3.38	0.20	0.285	0.016	0.036	0.010	4.03	0.20	−0.178	0.028	−0.011	0.010
1999 May 15	3.72	0.22	0.229	0.016	0.042	0.010	4.17	0.21	−0.174	0.027	−0.032	0.010
1999 Sep 18	4.91	0.43	0.194	0.019	0.057	0.012	4.97	0.34	−0.218	0.047	−0.036	0.016
1999 Dec 9	3.03	0.16	0.321	0.015	0.048	0.011	4.06	0.21	−0.157	0.021	−0.004	0.010
2000 May 15	3.48	0.19	0.214	0.015	0.012	0.010	3.15	0.17	−0.403	0.028	0.021	0.013
2000 Aug 7	4.53	0.28	0.002	0.019	0.014	0.013	2.36	0.12	−0.652	0.076	0.002	0.017
2000 Nov 5	4.21	0.24	0.089	0.015	0.065	0.012	1.97	0.10	−0.490	0.066	−0.003	0.016
2000 Nov 6	4.63	0.25	0.139	0.017	0.024	0.015	1.87	0.10	−0.565	0.049	−0.037	0.013
2001 Mar 31	3.54	0.23	0.212	0.021	0.012	0.010	3.62	0.21	−0.225	0.034	−0.054	0.016
2001 Jun 29	3.82	0.40	0.285	0.041	0.029	0.013	3.82	0.26	−0.259	0.082	−0.021	0.019
2001 Oct 19	3.52	0.21	0.193	0.017	0.075	0.011	3.00	0.15	−0.390	0.042	0.010	0.020
2001 Dec 21	4.34	0.28	0.176	0.023	0.016	0.011	2.48	0.14	−0.507	0.077	−0.055	0.010
2002 Apr 14	3.58	0.18	0.165	0.015	0.055	0.010	2.59	0.13	−0.385	0.016	−0.058	0.011
2002 Jul 14	2.88	0.30	0.315	0.033	0.049	0.010	3.42	0.19	−0.191	0.068	−0.053	0.023
2002 Nov 20	2.62	0.23	0.439	0.039	0.086	0.010	4.23	0.23	−0.132	0.048	−0.003	0.013
2003 Jan 26	2.72	0.26	0.448	0.033	0.138	0.010	4.59	0.23	−0.145	0.056	0.012	0.016
2003 May 18	2.81	0.15	0.600	0.015	0.086	0.011	3.84	0.19	−0.094	0.022	0.022	0.011
2003 Sep 8	3.02	0.18	0.648	0.016	0.106	0.011	3.26	0.18	−0.066	0.032	0.019	0.012
2003 Dec 5	3.20	0.16	0.175	0.015	0.009	0.011	2.84	0.14	−0.548	0.019	−0.087	0.010
2004 Mar 6	3.13	0.16	0.189	0.015	0.069	0.011	2.51	0.13	−0.504	0.023	−0.033	0.014
2004 May 18	2.58	0.15	0.041	0.016	−0.122	0.010	2.51	0.13	−0.640	0.039	−0.264	0.018
2004 Jun 26	2.55	0.25	0.376	0.027	0.064	0.011	2.41	0.12	−0.324	0.109	−0.078	0.021
2004 Dec 11	2.62	0.14	0.113	0.018	0.029	0.010	2.90	0.15	−0.565	0.032	−0.041	0.013
2005 Jan 15	2.64	0.14	0.033	0.018	0.080	0.010	2.92	0.15	−0.651	0.030	0.028	0.014
2005 May 28	2.90	0.15	−0.005	0.015	0.060	0.010	2.79	0.14	−0.701	0.021	0.020	0.011
2005 Jul 16	2.74	0.14	−0.008	0.015	0.011	0.010	2.71	0.14	−0.732	0.023	−0.022	0.011

Notes. Columns 1 and 2: flux density and flux-density standard error of component C1; Columns 3–6: position (α and δ), relative to image phase center (see definition in the text), and position standard error of component C1; Columns 7 and 8: flux density and flux-density standard error of component C2; Columns 9–12: position (α and δ), relative to image phase center, and position standard error of component C2. The tabulated flux-density standard errors do not include the estimated 10% standard error in the VLBI flux-density scale at each epoch.

likewise that of component C2 to the "stationary" component, we used the results from the studies of Jorstad et al. (2001, 2005) to simulate 8.4 GHz images of the core region of 3C 454.3. In particular, we used model data for the core, "stationary" component, and moving jet components at nine epochs, each within 30 days of one of our observations (see Table 5). We retained the nominal position of each 43 GHz component at each epoch, but modified the flux densities of the components in approximate accordance with spectra presented in the literature (e.g., Pagels et al. 2004; Chen et al. 2005; Krichbaum et al. 2006a). We generated the simulated 8.4 GHz image for each of the relevant epochs by (1) Fourier-transforming the flux-density-adjusted 43 GHz model onto a spatial frequency "grid" corresponding to our 8.4 GHz $u-v$ coverage, (2) imaging (i.e., Fourier-inverting and deconvolving with the CLEAN algorithm) the "gridded" data using the same restoring beam as for the actual 8.4 GHz image, (3) fitting the two-point-source model (described previously) to the image, and finally (4) repeating steps 1–3, tweaking the flux densities of the 43 GHz model components, until the flux densities and separation of the two point sources in the simulated 8.4 GHz image agreed with those in the actual 8.4 GHz image to approximately within the errors given in Table 4. For illustrative purposes we present in Figure 5 the simulated image and corresponding actual image for one of the nine epoch pairs. We give the results of the two-component model for the simulated image at each of the nine epochs in Table 5. We refer to the simulated easternmost component as $C1_s$ and the simulated westernmost component as $C2_s$. All positions in the table are given with respect to the 43 GHz core position. The fit position of $C1_s$ (Columns 1 and 2 in Table 5) therefore explicitly gives the offset (in each coordinate) of this component from the 43 GHz core. The mean $C1_s$–core displacement is 0.18 ± 0.06 mas toward the west, where the uncertainty represents the rms variation in the position of $C1_s$. We note that the largest displacements occur shortly after the ejection of new jet components, when the

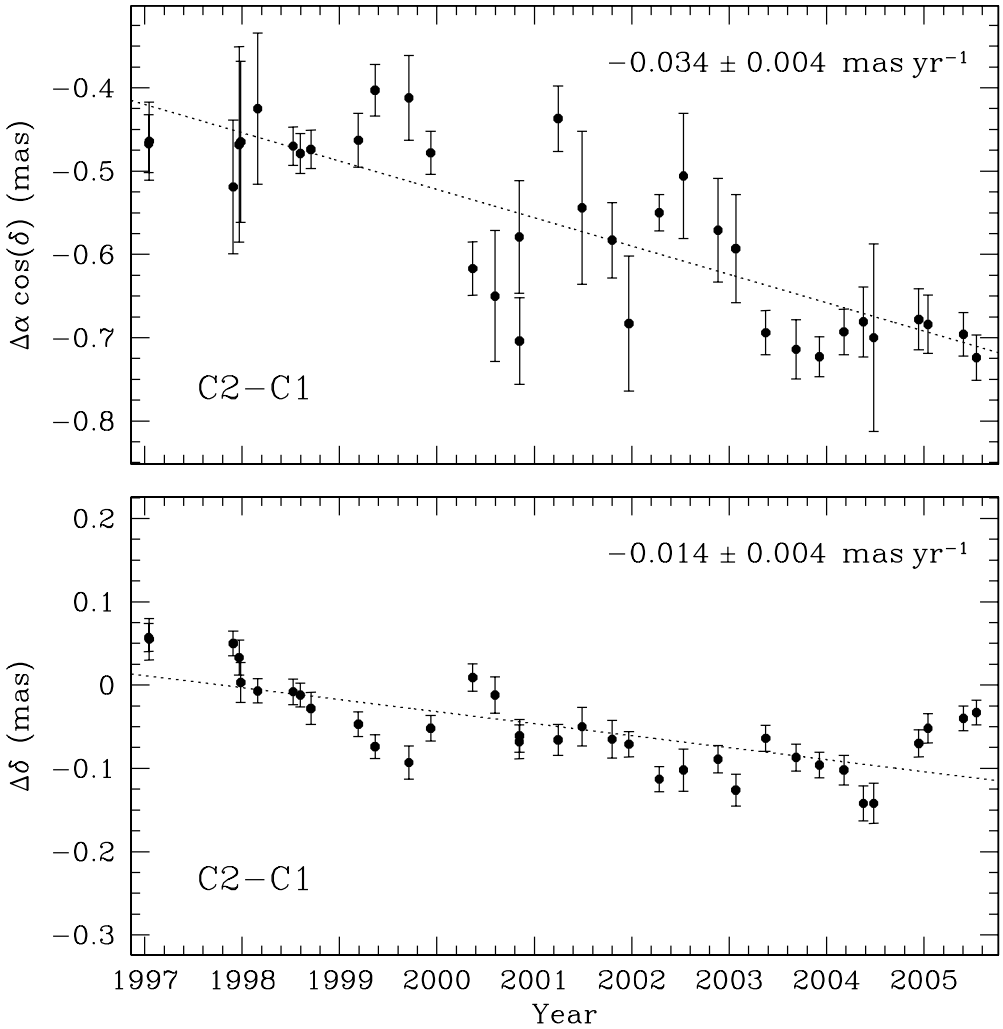

Figure 4. Position of 3C 454.3 core-region model component C2 relative to core-region model component C1. Error bars are the root-sum-square (rss) of the standard errors in the position estimates of C1 and C2. Our estimated proper motion of C2 relative to C1 is indicated by the dotted lines. Note that the residuals are not distributed randomly about the straight lines. The apparent "oscillations" may represent real epoch-to-epoch changes in the separation of C2 from C1, due to changes in the unresolved structure in the core region (see Section 5.2.1).

Table 5
3C 454.3 Simulated-image Component Positions

43 GHz Epoch	8.4 GHz Epoch	$C1_s$–Core $\Delta\alpha$ (mas) [1]	$C1_s$–Core $\Delta\delta$ (mas) [2]	$C2_s$–Core $\Delta\alpha$ (mas) [3]	$C2_s$–Core $\Delta\delta$ (mas) [4]	$C2_s$–Stat $\Delta\alpha$ (mas) [5]	$C2_s$–Stat $\Delta\delta$ (mas) [6]
1996 Dec 23	1997 Jan 16	−0.12	0.03	−0.60	0.14	0.05	−0.06
1998 Mar 25	1998 Mar 1	−0.07	0.00	−0.54	0.07	−0.05	0.00
1998 Aug 1	1998 Aug 8	−0.21	0.11	−0.72	0.16	−0.11	−0.02
1998 Oct 5	1998 Sep 16	−0.23	0.08	−0.75	0.05	−0.03	0.01
1999 Apr 29	1999 May 15	−0.25	0.00	−0.65	0.10	−0.01	−0.01
1999 Oct 6	1999 Sep 18	−0.22	0.05	−0.73	0.06	−0.08	−0.01
1999 Dec 5	1999 Dec 9	−0.16	0.01	−0.68	0.04	−0.01	0.00
2000 Jul 17	2000 Aug 7	−0.19	0.00	−0.84	−0.01	−0.23	−0.09
2001 Apr 14	2001 Mar 31	−0.20	0.00	−0.67	−0.09	−0.03	0.01

Notes. Columns 1 and 2: position (α and δ) of simulated 8.4 GHz component $C1_s$ relative to the 43 GHz core; Columns 3 and 4: position (α and δ) of simulated 8.4 GHz component $C2_s$ relative to the 43 GHz core; Columns 5 and 6: position (α and δ) of simulated 8.4 GHz component $C2_s$ relative to the 43 GHz "stationary" component.

flux density of the core is relatively low compared with that of the jet component (see Figure 5). Columns 5 and 6 in Table 5 give the offset in each coordinate of $C2_s$ from the 43 GHz "stationary" component. The mean $C2_s$–stationary-component displacement is 0.06 ± 0.08 mas toward the west-southwest. The smaller value of this displacement, compared with the $C1_s$–core displacement, is reasonable, since jet components move both into and out of the position defined by the "stationary" component, whereas jet components move only westward away from the core. The larger peak-to-peak variations in the $C2_s$–stationary-component displacement, compared with the $C1_s$–core displacement (see Table 5), reflect the complexity of the structure seen at 43 GHz at the western end of the core region.

5.2.2. Inner-jet Region

Our images of 3C 454.3 show that new components occasionally emerge to the west or southwest of the position approximately defined by core-region component C2, and move through the inner-jet region toward the extended jet. At any given epoch, the inner-jet region itself may contain zero, one, or multiple components in transit between the core region and extended jet. Unfortunately, given the general complexity of the radio structure in the inner-jet region, the relative weakness

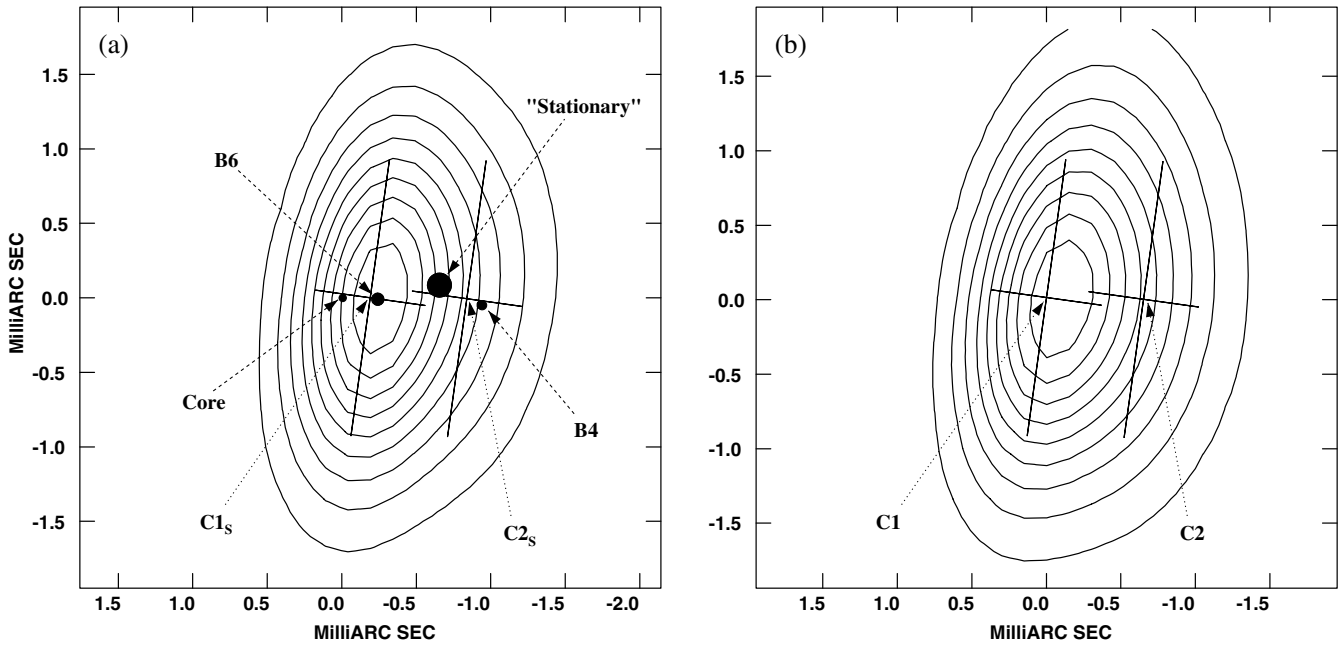

Figure 5. (a) Simulated 8.4 GHz image for 2000 July 17 and (b) actual 8.4 GHz image ("zoomed-in" on the core region) for 2000 August 7. Contour levels are 10%, 20%, 30%, 40%, 50%, 60%, 70%, 80%, and 90% of the peak brightness in each image. The 43 GHz model for 2000 July 17 (see Jorstad et al. 2005), upon which the simulated image is based, consists of four components (filled black circles): Core, B6, "Stationary," and B4. With the exception of the Core, the size of the circle represents the diameter (FWHM) of the component. The Core is modeled as a point source. The positions of 8.4 GHz model components $C1_s$ and $C2_s$ in (a) and C1 and C2 in (b) are indicated by crosses which reflect the size and orientation of the restoring beam. The restoring beam is the same for both images. The images are centered on the center of $C1_s$ in (a) and C1 in (b).

of the components, and the resolution of our VLBI arrays, we were able to confidently "isolate" inner-jet-region components for only a limited number of epochs (see below).

To estimate the proper motion (relative to C1) of components transitioning between the core region and inner-jet region, we attempted, as described in Section 5.2.1, to simultaneously describe the core-region components and a transition component by fitting a three point-source model to the easternmost ∼2 mas of the 3C 454.3 radio structure. For 22 of the 35 epochs, we found the fit positions and flux densities of core-region components C1′ and C2′ in the three-component model to differ significantly (i.e., by more than two times the respective standard errors given in Table 4) from those of C1 and C2 in the two-component model. Moreover, we found that the position of C1′ for these 22 epochs did not align with the features seen in the images; specifically, C1′ was positioned too far east to produce the sharp cutoff seen at the eastern edge of the source. We therefore consider the three-component model unacceptable for these epochs. Of the 13 epochs with acceptably fit models, 11 fall within the ∼2.5 yr interval from 2003 January to 2005 July. For these 11 epochs, we repeated the three-component fit but with the position of C1′ fixed to the position of C1 found in the two-component model. We plot in Figure 6 the separation from C1 of the 0.6 ± 0.1 Jy transition component, D1. We determined for the 11 epochs a relative proper motion for D1 with respect to C1 of -0.123 ± 0.018 mas yr^{-1} in α and -0.071 ± 0.015 mas yr^{-1} in δ.

We were also able to track the motion of a second component, D2, for seven consecutive epochs from 2004 March to 2005 July, by fitting a model consisting of a single point source (D2) to the ∼2 mas wide portion of the inner-jet region west of D1. We plot in Figure 6 the separation from C1 of the 0.05 ± 0.01 Jy D2. We determined for the seven epochs a relative proper motion for D2 with respect to C1 of -0.141 ± 0.037 mas yr^{-1} in α and $+0.157 \pm 0.041$ mas yr^{-1} in δ.

While the proper motion in α is similar for components D1 and D2, the difference in the proper motion in δ from a negative value for D1 to a positive value for D2 clearly demonstrates a bend in the jet between these components. A similar bend in the inner-jet region was noted by Pauliny-Toth (1998) for a component at 5 and 8.4 GHz that moved from a position (relative to their "core") near that of D1 (relative to C1) to a position beyond that of D2. The bend demonstrated by component motion is also clearly observed in the low-surface-brightness emission in VLBI images between 5 and 15 GHz (Cawthorne & Gabuzda 1996; Pauliny-Toth 1998; Kellermann et al. 1998; Chen et al. 2005; Lister et al. 2009). The magnitudes of the proper motions of D1 and D2 are a factor of two to four lower than those seen at 5 and 8.4 GHz for a component traversing a region 1.5–5.0 mas west of the core between 1983 and 1991 (Pauliny-Toth 1998), but consistent with those seen at 15 GHz for a component traversing a region 2.5–3.5 mas west of the core between 2006 and 2009 (see Vercellone et al. 2010).

5.2.3. Extended-jet Region

Beyond the brightness peak ∼5.5 mas west of component C1, the extended jet of 3C 454.3 has no clearly discernible subcomponents, at least none that can be traced from epoch to epoch. We fit to the extended-jet region at each epoch a model consisting of a point source and an elliptical Gaussian, representing, respectively, the compact emission component near the (jet) brightness peak and the ∼6.5 mas (mean major-axis length) extended jet itself. The results of the fit are given in Table 6. We refer to the compact component as J1 and the extended component as Jext. The uncertainties in the major axis, minor axis, and P.A. of Jext are statistical standard errors.

In Figure 7, we plot the separations at each epoch of J1 from C1 and the peak of Jext from C1. We see that J1 moved ∼0.7 mas relative to C1 over the ∼8.5 yr period of our observing program, largely in the δ coordinate. We determined a mean relative proper

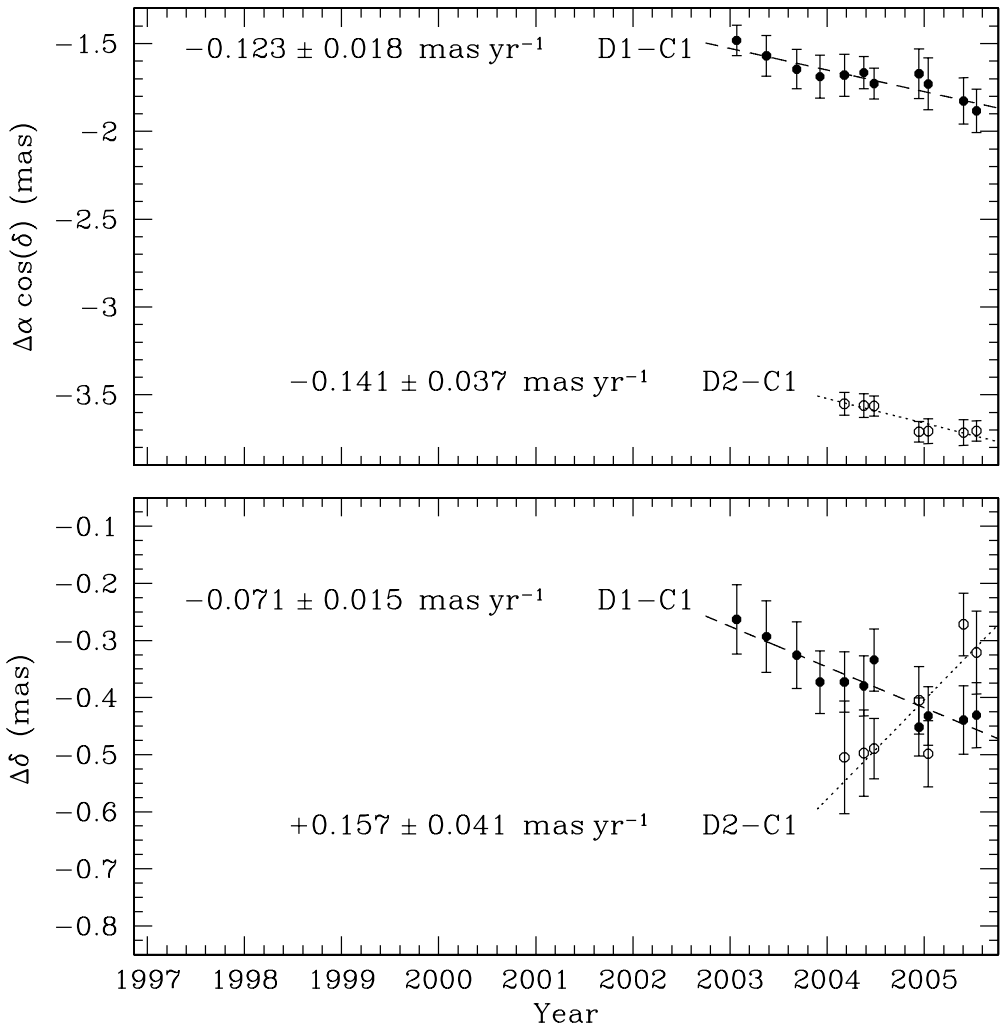

Figure 6. Positions of 3C 454.3 inner-jet model components D1 (filled circles) and D2 (open circles) relative to core-region model component C1. Error bars are the rss of the standard errors in the position estimates of C1 and D1 or D2, as appropriate. The proper motions of D1 and D2 relative to C1 are indicated by the dashed and dotted lines. Note that different scales are used for the α and δ coordinates.

motion for J1 with respect to C1 of -0.031 ± 0.004 mas yr^{-1} in α and $+0.083 \pm 0.004$ mas yr^{-1} in δ. The proper motion of J1 (see Figure 7), though approximately uniform in α, changed in δ between the first 26 epochs ($\sim$6.5 yr) and the remaining nine epochs ($\sim$2.0 yr). Fitting to each time period separately, we determined the relative proper motion in δ to decrease from $+0.104 \pm 0.006$ mas yr^{-1} for the first 26 epochs to $+0.002 \pm 0.021$ mas yr^{-1} for the remaining nine. The result for the first 26 epochs suggests that the northward bend in the jet that starts at a position $\sim$3 mas west of C1, i.e., at a position between transient components D1 and D2, continues to a position $\sim$5.6 mas west of C1. The rapid change at this point in the direction of the proper motion may signify a second sharp bend in the jet. Additionally, the drastic decrease at this point in the magnitude of the proper motion could indicate a transition away from the highly collimated flow seen in the core and inner-jet regions.

Figure 7 shows that the peak of Jext moved northwest $\sim$1.1 mas relative to C1 over the $\sim$8.5 yr period of our observing program. We determined a relative proper motion for the peak of Jext with respect to C1 of -0.084 ± 0.006 mas yr^{-1} in α and $+0.095 \pm 0.006$ mas yr^{-1} in δ. The proper motion of the peak of Jext (along P.A. $= -41^\circ \pm 3^\circ$) was precisely aligned with the component's major axis (P.A. $= -40^\circ \pm 1^\circ$). This result is consistent with the 1.7 GHz space-VLBI observations of Chen et al. (2005), which showed for an epoch in 1999 June that the extended jet region was composed of three or four components. Moreover, the decrease in the major-axis length (FWHM) of the "moving" Jext from $\sim$7.3 mas to $\sim$5.9 mas (see Table 6) suggests that no "new" component transited from the inner-jet region to the extended-jet region during our $\sim$8.5 yr observing period. Component J1, as discussed above, may have been close to this transition near the end of our program. We note that the major axis of Jext is approximately aligned with the axis of the arcsecond-scale jet of 3C 454.3 (see Cheung et al. 2005), suggesting that the trajectory directions of components beyond J1 are roughly constant over $\sim$5.″2 ($\sim$40 kpc).

5.2.4. Deconvolution Errors

Deconvolution errors are known to limit the fidelity of images produced using the CLEAN deconvolution algorithm (see, e.g., Briggs 1995; Briggs et al. 1999). We performed two tests to investigate the reliability of the radio structure seen in the CLEAN deconvolved images of 3C 454.3. The first test was a simulation study in which we produced u–v data on a "grid"

Table 6
3C 454.3 Image Plane 8.4 GHz Model Parameters: Extended-jet Region

Start Date	Component J1						Component Jext											
	$S_{8.4}$ (Jy) [1]	σ_S (Jy) [2]	$\Delta\alpha$ (mas) [3]	σ_α (mas) [4]	$\Delta\delta$ (mas) [5]	σ_δ (mas) [6]	$S_{8.4}$ (Jy) [7]	σ_S (Jy) [8]	$\Delta\alpha$ (mas) [9]	σ_α (mas) [10]	$\Delta\delta$ (mas) [11]	σ_δ (mas) [12]	Maj (mas) [13]	$\sigma_{\rm Maj}$ (mas) [14]	Min (mas) [15]	$\sigma_{\rm Min}$ (mas) [16]	p.a. (°) [17]	$\sigma_{\rm p.a.}$ (°) [18]
1997 Jan 16	0.267	0.027	−5.343	0.055	0.329	0.077	1.32	0.07	−6.075	0.045	1.650	0.046	7.28	0.10	1.77	0.11	−40.5	0.7
1997 Jan 18	0.263	0.026	−5.366	0.058	0.341	0.079	1.34	0.07	−6.093	0.055	1.674	0.057	7.43	0.13	1.78	0.15	−41.1	0.9
1997 Nov 29	0.357	0.036	−5.354	0.054	0.454	0.073	1.51	0.08	−6.201	0.043	1.894	0.044	7.53	0.09	1.87	0.12	−41.5	0.7
1997 Dec 21	0.332	0.033	−5.399	0.065	0.449	0.073	1.58	0.09	−6.174	0.066	1.854	0.061	7.29	0.15	1.83	0.19	−40.7	1.1
1997 Dec 27	0.308	0.031	−5.377	0.059	0.443	0.073	1.47	0.08	−6.195	0.049	1.840	0.045	7.02	0.09	1.85	0.11	−40.1	0.7
1998 Mar 1	0.284	0.028	−5.410	0.062	0.439	0.073	1.48	0.08	−6.063	0.051	1.695	0.041	7.09	0.08	1.74	0.09	−40.6	0.6
1998 Jul 12	0.276	0.028	−5.486	0.055	0.460	0.086	1.28	0.07	−6.307	0.045	1.911	0.048	6.78	0.11	1.82	0.15	−41.2	1.0
1998 Aug 8	0.275	0.028	−5.488	0.054	0.463	0.090	1.41	0.07	−6.140	0.042	1.726	0.045	6.49	0.10	1.83	0.14	−38.8	1.0
1998 Sep 16	0.298	0.030	−5.466	0.053	0.473	0.084	1.46	0.07	−6.236	0.040	1.841	0.042	6.99	0.08	1.89	0.11	−40.5	0.7
1999 Mar 13	0.238	0.024	−5.418	0.053	0.506	0.077	1.33	0.07	−6.245	0.045	1.885	0.048	6.45	0.11	1.77	0.15	−40.2	1.0
1999 May 15	0.246	0.025	−5.365	0.054	0.491	0.070	1.40	0.07	−6.180	0.047	1.840	0.049	6.28	0.12	1.78	0.15	−39.5	1.1
1999 Sep 18	0.297	0.030	−5.393	0.055	0.507	0.080	1.54	0.08	−6.273	0.049	1.903	0.051	6.26	0.12	1.88	0.17	−40.5	1.3
1999 Dec 9	0.269	0.027	−5.465	0.056	0.548	0.081	1.34	0.07	−6.399	0.042	2.028	0.045	6.31	0.09	1.91	0.14	−40.8	1.0
2000 May 15	0.226	0.023	−5.540	0.069	0.717	0.058	1.45	0.07	−6.405	0.038	1.893	0.039	6.29	0.06	1.86	0.09	−37.9	0.6
2000 Aug 7	0.240	0.024	−5.513	0.074	0.721	0.073	1.43	0.07	−6.459	0.041	2.076	0.041	6.48	0.07	1.94	0.11	−40.3	0.8
2000 Nov 5	0.217	0.022	−5.427	0.068	0.710	0.068	1.41	0.07	−6.274	0.040	1.926	0.041	6.07	0.08	1.84	0.11	−39.9	0.8
2000 Nov 6	0.310	0.031	−5.494	0.057	0.709	0.080	1.35	0.07	−6.577	0.045	2.372	0.048	6.13	0.10	2.08	0.16	−40.4	1.2
2001 Mar 31	0.243	0.024	−5.487	0.061	0.770	0.061	1.27	0.07	−6.549	0.043	2.147	0.043	6.18	0.09	1.78	0.12	−38.8	0.9
2001 Jun 29	0.207	0.021	−5.521	0.076	0.811	0.069	1.29	0.07	−6.458	0.053	2.084	0.040	5.78	0.07	1.87	0.11	−38.2	0.9
2001 Oct 19	0.222	0.022	−5.532	0.068	0.864	0.081	1.47	0.08	−6.557	0.048	2.275	0.054	6.34	0.13	1.98	0.19	−38.2	1.4
2001 Dec 21	0.244	0.024	−5.540	0.063	0.848	0.077	1.32	0.07	−6.594	0.043	2.340	0.040	6.08	0.07	1.96	0.11	−39.8	0.8
2002 Apr 14	0.241	0.024	−5.489	0.071	0.937	0.092	1.29	0.07	−6.554	0.040	2.287	0.042	5.92	0.09	1.98	0.15	−39.0	1.2
2002 Jul 14	0.194	0.019	−5.491	0.068	0.876	0.066	1.43	0.07	−6.557	0.048	2.237	0.039	6.02	0.07	1.85	0.10	−39.2	0.8
2002 Nov 20	0.199	0.020	−5.587	0.072	0.929	0.075	1.28	0.07	−6.672	0.053	2.379	0.039	5.95	0.07	1.84	0.11	−39.9	0.8
2003 Jan 26	0.183	0.018	−5.569	0.079	0.887	0.077	1.40	0.07	−6.593	0.050	2.216	0.044	5.79	0.09	1.82	0.14	−40.5	1.2
2003 May 18	0.169	0.017	−5.693	0.058	0.983	0.078	1.30	0.07	−6.648	0.039	2.250	0.041	5.54	0.07	1.80	0.12	−38.8	1.0
2003 Sep 8	0.144	0.015	−5.628	0.099	0.976	0.080	1.30	0.07	−6.633	0.043	2.261	0.045	5.56	0.09	1.73	0.14	−39.1	1.1
2003 Dec 5	0.175	0.018	−5.582	0.070	0.927	0.076	1.42	0.07	−6.621	0.039	2.267	0.040	5.81	0.07	1.78	0.11	−39.1	0.8
2004 Mar 6	0.176	0.018	−5.577	0.063	0.951	0.081	1.49	0.08	−6.634	0.040	2.375	0.042	6.05	0.08	1.86	0.12	−40.0	0.9
2004 May 18	0.194	0.019	−5.577	0.088	0.944	0.092	1.44	0.07	−6.693	0.038	2.441	0.039	5.86	0.07	1.91	0.11	−40.3	0.9
2004 Jun 26	0.166	0.017	−5.480	0.084	0.946	0.072	1.40	0.07	−6.598	0.042	2.346	0.034	5.80	0.04	1.82	0.05	−39.5	0.4
2004 Dec 11	0.176	0.018	−5.628	0.074	0.931	0.077	1.39	0.07	−6.782	0.036	2.440	0.033	5.99	0.03	1.85	0.05	−40.5	0.4
2005 Jan 15	0.181	0.018	−5.635	0.067	0.936	0.075	1.36	0.07	−6.811	0.037	2.469	0.035	5.90	0.04	1.86	0.07	−40.9	0.5
2005 May 28	0.189	0.019	−5.633	0.066	0.978	0.076	1.38	0.07	−6.756	0.037	2.476	0.037	5.80	0.06	1.83	0.08	−40.3	0.7
2005 Jul 16	0.187	0.019	−5.657	0.065	0.955	0.083	1.37	0.07	−6.821	0.034	2.506	0.033	5.87	0.03	1.84	0.05	−40.9	0.4

Notes. Columns 1 and 2: flux density and flux-density standard error of component J1; Columns 3–6: position (α and δ), relative to component C1, and position standard error of component J1; Columns 7 and 8: integrated flux density and flux-density standard error of component Jext; Columns 9–12: position (α and δ), relative to component C1, and position standard error of the peak of component Jext; Columns 13 and 14: major-axis length (FWHM) and major-axis-length statistical standard error of component Jext; Columns 15 and 16: minor-axis length (FWHM) and minor-axis-length statistical standard error of component Jext; Columns 17 and 18: position angle (east of north) of major axis, and position-angle statistical standard error, of component Jext. The tabulated flux-density standard errors do not include the estimated 10% standard error in the VLBI flux-density scale at each epoch.

corresponding to our typical[10] u–v coverage and consisting of the Fourier transforms of simple geometrical models similar to 3C 454.3 as described in Sections 5.2.1–5.2.3. Each variation of the model used different positions and flux densities for the two bright core-region components (C1 and C2), and in a few cases also used different positions and flux densities for the weaker components (D1, D2, J1, and Jext). We Fourier-inverted the simulated data for each variation and used the CLEAN deconvolution algorithm to produce images. We subsequently compared to the input models the resulting simulated images and new models fit to the simulated images. (The new model, or "output" model, contains the same number and type of components as the input model.) For each variation of the input model, we found the model structure to be reasonably well reproduced in the simulated images (taking into account the size and orientation of the CLEAN restoring beam), but noted that additional "ripples" were present in the core region with peak-to-peak amplitudes of 1%–3% of the image peak and in the inner-jet and extended-jet regions with amplitudes of 0.2%–1% of the image peak. The Fourier counterparts of these ripples occur at spatial frequencies just outside the bulk of the u–v coverage. The maximum fraction (considering several variations of the input model) of the rms flux density in ripples near the positions of the input-model components to the flux density in the components themselves was ∼5% for the core-region components (C1 and C2) and extended-jet component (Jext) and ∼10% for the compact-jet components (D1, D2, and J1). When we compared the flux densities of the output-model components to those of the input-model

[10] We take as our typical u–v coverage that of epoch 2003 May 18 (see Table 1). We repeated the simulation study described here for nontypical instances of our u–v coverage (1997 January 18, 2002 April 14, and 2002 November 20) and found flux-density and position variations for the 3C 454.3 model components consistent with the uncertainties derived here for the typical coverage.

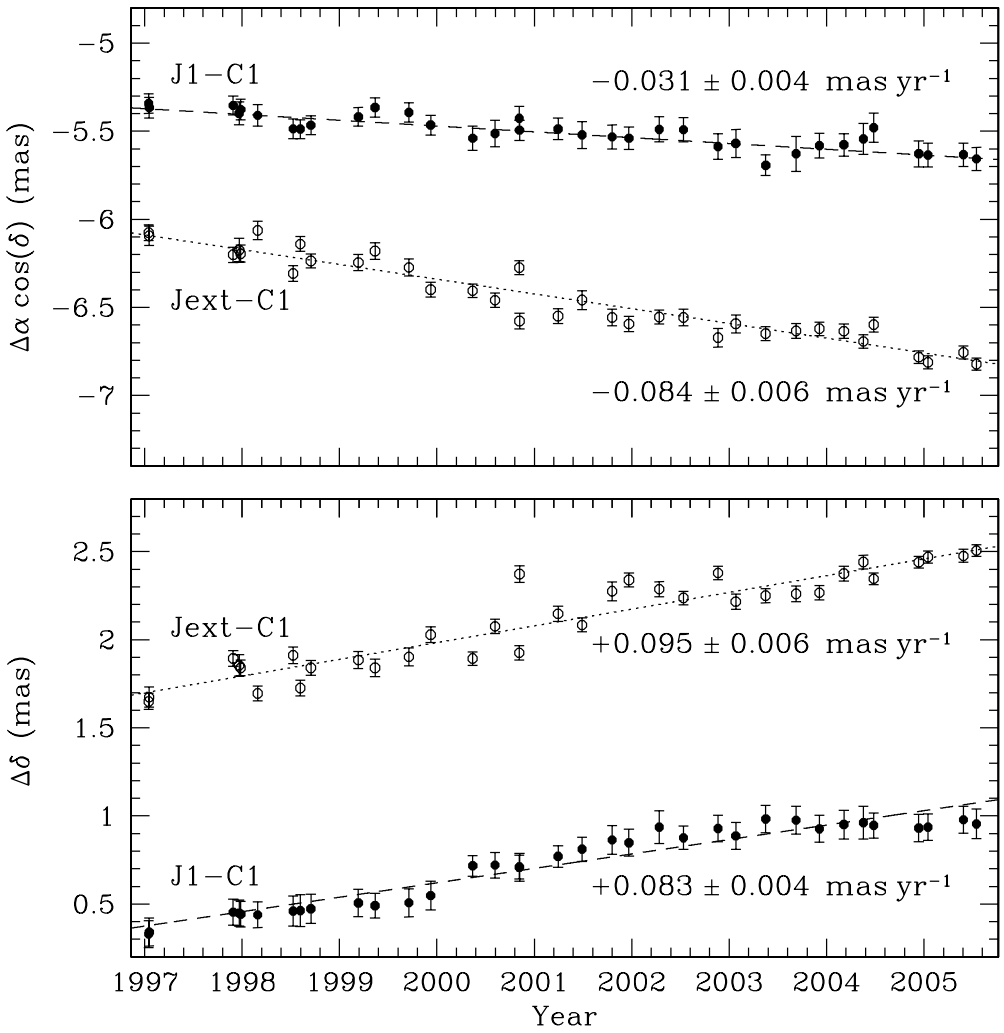

Figure 7. Positions of 3C 454.3 extended-jet model components J1 (filled circles) and Jext (open circles) relative to core-region model component C1. Error bars are the rss of the standard errors in the position estimates of C1 and J1 or Jext, as appropriate. Note, the larger error bars for the relative J1 positions, compared to those for the relative Jext positions, reflect in part the ∼70% larger deconvolution errors in the former (see Section 5.2.4). The mean proper motions of J1 and Jext relative to C1 are indicated by the dashed and dotted lines.

components, we found corresponding differences of up to ∼5% for C1, C2, and Jext and ∼10% for D1, D2, and J1. We therefore take these values (∼5% for each of C1, C2, and Jext and ∼10% for each of D1, D2, and J1) as a conservative estimate of the fractional flux-density uncertainty due to deconvolution errors. To estimate the amount by which the ripples affect the positions of the model components, we compared the positions of the output and input model components for each variation. We found the maximum difference between the output and input component positions to be ∼0.020 mas for C1 and C2 (∼0.015 mas in α and ∼0.010 mas in δ), ∼0.100 mas for D1 (∼0.080 mas in α and ∼0.050 mas in δ), ∼0.070 mas for D2 and J1 (∼0.050 mas in each coordinate), and ∼0.040 mas for Jext (∼0.030 mas in each coordinate). We take the maximum difference between the positions of the output and input model components quoted above as conservative estimates of the various position uncertainties due to deconvolution errors.

As a second reliability test we used another deconvolution algorithm, namely the maximum entropy method (MEM; e.g., Cornwell et al. 1999), to produce images of 3C 454.3 at select epochs. We then performed the same fits in the image plane as described in Sections 5.2.1–5.2.3. We found that the differences in the position determinations of the relevant components in the MEM deconvolved images compared to the CLEAN deconvolved images were well within the limits given above.

5.3. *u–v*-plane Model Fitting at 8.4 GHz

We also performed an analysis of the changing 8.4 GHz radio structure of 3C 454.3 via model fitting in the *u–v* plane. Fitting in the *u–v* plane is not affected by deconvolution errors (as described in Section 5.2.4) and is not as sensitive to differences from epoch to epoch in the precise *u–v* coverage. However, we cannot, given our *u–v* coverage, simultaneously constrain the high-flux-density components in the core region and the low-flux-density or low-surface-brightness components in the inner-jet and extended-jet regions. We fit to the *u–v* data at each epoch a model consisting of three point sources, which describe, approximately, the core-region components C1 and C2 as well as the compact jet component J1 (see Section 5.2). For comparison with the image-plane models, we plot in Figure 8 the separations in the *u–v*-plane model of $C2_{u-v}$ and $C1_{u-v}$ (top panels) and $J1_{u-v}$ and $C1_{u-v}$ (bottom panels). The proper motion of $C2_{u-v}$ with respect to $C1_{u-v}$ is consistent with that found in the image-plane analysis. The proper motion of $J1_{u-v}$ with respect to $C1_{u-v}$ differs at the 1.5σ level from that

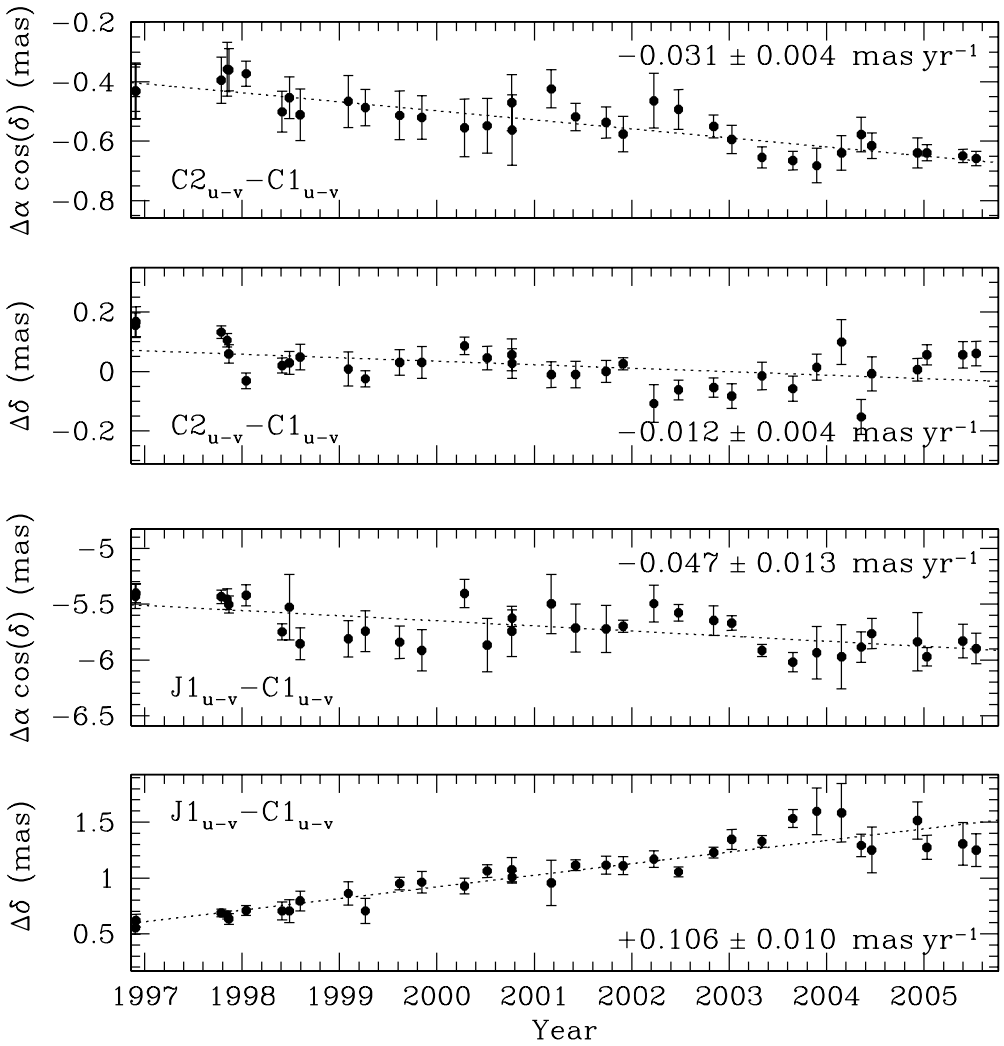

Figure 8. Positions of 3C 454.3 u–v-plane-based model components C2$_{u-v}$ (top panels) and J1$_{u-v}$ (bottom panels) relative to C1$_{u-v}$. Error bars are the rss of the statistical errors in the position estimates of each pair of components. The proper motions of C2$_{u-v}$ and J1$_{u-v}$ relative to C1$_{u-v}$ are indicated by dotted lines. The uncertainties quoted in the proper motion values are statistical errors. Note that different scales are used for the C2$_{u-v}$–C1$_{u-v}$ and J1$_{u-v}$–C1$_{u-v}$ positions.

found in the image-plane analysis. This difference may result from structural changes in the unmodeled extended jet over the ∼8.5 yr period of our observing program. Given the limitations of the u–v-plane-based analysis for 3C 454.3, we believe our image-plane models (see Section 5.2) provide the better overall description of the evolving structure of this source.

5.4. VLBI Images at 5.0 and 15.4 GHz

We present in Figure 9 the 5.0, 8.4, and 15.4 GHz images of 3C 454.3 generated from our nearly simultaneous VLBI observations on 2004 May 18 (see Section 3). The 8.4 GHz image is the same as that presented in Figure 2 except for the choice of contour levels. The images are aligned on the center of the easternmost component of the radio structure (see below). The image characteristics are given in Table 3. The 5.0 and 15.4 GHz images are slightly noisier than the 8.4 GHz image, mainly because the total time on source was ∼4 hr at each of 5.0 and 15.4 GHz compared to ∼7 hr at 8.4 GHz. Nevertheless, the images at all three frequencies show a core region extended nearly east–west and a jet bending toward the north. To quantitatively compare the positions and flux densities of the core- and inner-jet-region components, we fit to the combined core/inner-jet region in each of the 5.0 and 15.4 GHz images the three-component model (C1, C2, and D1) described in Section 5.2.2. Similarly, to compare the positions and flux densities of the extended-jet-region component(s), we fit to the extended-jet region in the 5.0 GHz image the two-component model (J1 and Jext) described in Section 5.2.3. However, at 15.4 GHz we fit only a single point source (J1) to the region within ∼2 mas of the jet peak, because the surface brightness of the extended jet in this image is too low to allow us to adequately constrain an elliptical Gaussian component. The results of the fits are given in Table 7 and illustrated in Figure 9. The uncertainties in the flux densities and positions include contributions, added in quadrature, of the statistical standard error of the fit and an estimate (using an analysis similar to that described in Section 5.2.4) of the systematic error associated with deconvolution errors in the corresponding image.

We choose in Figure 9 to align the images at each frequency on the (fit-estimated) center of component C1. This is a reasonable choice, since our comparison of the structure of the core region at 8.4 and 43 GHz in Section 5.2.1 shows that the 8.4 GHz C1 is located within ∼0.2 mas of the 43 GHz identified core. But how well do the images at 5.0, 8.4, and 15.4 GHz actually line-up? To answer this question we look at the separation of J1 and C1 at each frequency. The jet peak is clearly identified at

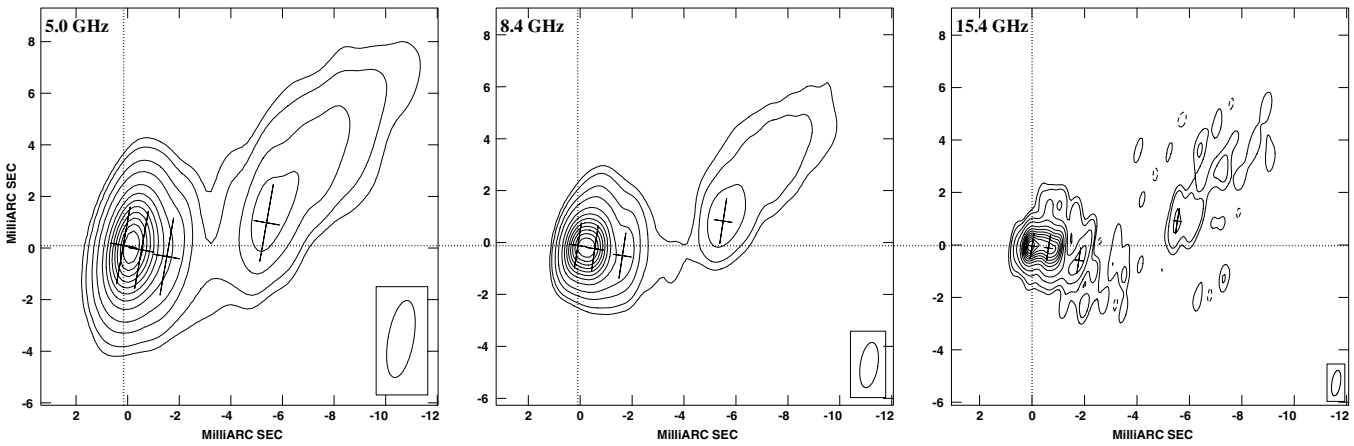

Figure 9. 5.0, 8.4, and 15.4 GHz VLBI images of 3C 454.3 for epoch 2004 May 18. In each image the contour levels are 1%, 2%, 5%, 10%, 20%, 30%, 40%, 50%, 60%, 70%, 80%, and 90% of the peak brightness. An additional contour, denoting −1% of the brightness peak, appears in the 15.4 GHz image. (Note, negative contour levels appear as dashed outlines.) Image characteristics are summarized in Table 3. The restoring beam is indicated in the bottom right-hand corner of each image. The images are aligned, as indicated by the dotted lines, on the center of component C1. The positions (from east to west) of components C1, C2, D1, and J1 (see Table 7) are indicated on each image by crosses which reflect the size and orientation of the restoring beam.

Table 7
3C 454.3 Image-plane Model Parameters for 2004 May 18

	Component C1		Component C2						Component D1						Component J1					
ν (GHz)	S_ν (Jy) [1]	σ_S (Jy) [2]	S_ν (Jy) [3]	σ_S (Jy) [4]	$\Delta\alpha$ (mas) [5]	σ_α (mas) [6]	$\Delta\delta$ (mas) [7]	σ_δ (mas) [8]	S_ν (Jy) [9]	σ_S (Jy) [10]	$\Delta\alpha$ (mas) [11]	σ_α (mas) [12]	$\Delta\delta$ (mas) [13]	σ_δ (mas) [14]	S_ν (Jy) [15]	σ_S (Jy) [16]	$\Delta\alpha$ (mas) [17]	σ_α (mas) [18]	$\Delta\delta$ (mas) [19]	σ_δ (mas) [20]
5.0	2.94	0.20	2.73	0.14	−0.701	0.022	−0.178	0.021	0.946	0.096	−1.685	0.081	−0.436	0.055	0.328	0.033	−5.553	0.052	0.878	0.061
8.4	2.42	0.15	2.45	0.13	−0.650	0.021	−0.120	0.016	0.621	0.078	−1.665	0.088	−0.380	0.053	0.194	0.019	−5.577	0.051	0.944	0.054
15.4	1.41	0.08	1.22	0.07	−0.626	0.018	−0.077	0.017	0.271	0.028	−1.782	0.052	−0.551	0.050	0.096	0.010	−5.544	0.036	0.950	0.045

Notes. Columns 1 and 2: flux density and flux-density standard error of component C1; Columns 3 and 4: flux density and flux-density standard error of component C2; Columns 5–8: position (α and δ), relative to component C1, and position standard error of component C2; Columns 9 and 10: flux density and flux-density standard error of component D1; Columns 11–14: position (α and δ), relative to component C1, and position standard error of component D1; Columns 15 and 16: flux density and flux-density standard error of component J1; Columns 17–20: position (α and δ), relative to component C1, and position standard error of component J1. The tabulated flux-density standard errors do not include the estimated 5% standard error in the VLBI flux-density scale for 2004 May 18 (see the text).

each frequency, and thus serves as a useful marker in the radio structure. The largest difference between the three images in the J1–C1 separation (see the last four columns of Table 7) is 0.033 ± 0.063 mas in α and 0.072 ± 0.076 mas in δ. We therefore believe that the images at 5.0, 8.4, and 15.4 GHz are aligned (relative to these internal reference points) to within 0.10 mas in α and 0.15 mas in δ; i.e., to better than ∼15% of the resolution of the 5.0 GHz image.

The separations of C2 and D1 from C1 are more variable with frequency than the separation of J1 from C1. This difference is not surprising considering the complexity of the underlying structure in the core and inner-jet regions. The ∼1.8 times higher angular resolution of the 15.4 GHz image, compared to that of the 8.4 GHz image, reveals that the core and inner-jet regions for 2004 May 18 contain more than three components. Specifically, there appears to be a component located between the positions of C1 and C2, and another component located west-southwest of the position of C2. Can we understand the differences in the fit-estimated C2–C1 and D1–C1 separations at each frequency in terms of the frequency-dependent flux densities of these unmodeled components? Generally speaking, the spectral index, α ($S \sim \nu^\alpha$), of a component is steeper (i.e., more negative) the farther west it is from the core (e.g., Pagels et al. 2004; Chen et al. 2005). Thus, relative to C1 and C2, a component lying between them will likely have a larger fractional flux density at 15.4 GHz than at 8.4 or 5.0 GHz, while a component west of C2 will have a larger fractional flux density at 5.0 GHz than at either 8.4 or 15.4 GHz. These flux-density differences would create at 15.4 GHz a "plateau" between C1 and C2 (as observed) and at 5.0 GHz a west-broadened C2. For a core-region modeled only by C1 and C2, we might then expect a C2–C1 separation which is smaller at 15.4 GHz than at 5.0 GHz. This is indeed what we find in our model fits (see Table 7). In the inner-jet region, the situation is reversed. Here, the component west-southwest of C2 might be expected to create at 5.0 GHz a plateau between C2 and D1, and yield a D1–C1 separation which is smaller at this frequency than at 15.4 GHz. These expectations, too, are confirmed by our model fits.

We give in Table 8 the flux-density ratio ($S_{\nu_{\rm high}}/S_{\nu_{\rm low}}$) and resulting point-to-point spectral index ($\alpha = \log(S_{\nu_{\rm high}}/S_{\nu_{\rm low}})/\log(\nu_{\rm high}/\nu_{\rm low})$) for each model component for each pair of frequencies. We also give for comparison the total (CLEAN) flux-density ratio (using the values in Table 3) and resulting point-to-point spectral index for each pair of frequencies. Note that to compute the standard errors in the flux densities, we added in quadrature to the other contributions a 5% uncertainty representative of the standard error in the VLBI flux-density scale. We adopt a 5% uncertainty for this epoch rather than the nominal 10% (see Section 4.3), because the VLBI- and VLA-determined flux densities at each frequency differ by only 2%–7% (see Table 3). The slightly lower ratio of VLBI-determined to VLA-determined flux density at 5.0 GHz compared to those at 8.4 and 15.4 GHz is likely due to the insensitivity of our VLBI observations to low-surface-brightness (and steep-spectral-index) emission in the extended jet at distances $\gtrsim$15 mas northwest of the core (see Chen et al. 2005).

Table 8
3C 454.3 Spectral Indices for 2004 May 18

ν_{high}/ν_{low} [1]	C1 [2]	α_{C1} [3]	C2 [4]	α_{C2} [5]	D1 [6]	α_{D1} [7]	J1 [8]	α_{J1} [9]	Total [10]	α_{Tot} [11]
8.4/5.0	0.823 ± 0.096	-0.38 ± 0.22	0.897 ± 0.097	-0.21 ± 0.20	0.656 ± 0.081	-0.81 ± 0.25	0.592 ± 0.093	-1.01 ± 0.30	0.864 ± 0.061	-0.28 ± 0.14
15.4/8.4	0.583 ± 0.064	-0.89 ± 0.19	0.498 ± 0.052	-1.14 ± 0.17	0.392 ± 0.061	-1.37 ± 0.28	0.495 ± 0.079	-1.16 ± 0.26	0.692 ± 0.049	-0.61 ± 0.12
15.4/5.0	0.480 ± 0.055	-0.65 ± 0.11	0.447 ± 0.046	-0.72 ± 0.09	0.287 ± 0.043	-1.11 ± 0.14	0.293 ± 0.047	-1.09 ± 0.14	0.598 ± 0.042	-0.46 ± 0.06

Notes. Column 1: frequency pair for which flux-density ratios and spectral indices are computed; Columns 2 and 3: flux-density ratio and point-to-point spectral index (see the text) for component C1; Columns 4 and 5: flux-density ratio and point-to-point spectral index for component C2; Columns 6 and 7: flux-density ratio and point-to-point spectral index for component D1; Columns 8 and 9: flux-density ratio and point-to-point spectral index for component J1; Columns 10 and 11: CLEAN flux-density ratio and point-to-point spectral index.

The spectral indices for C1, C2, and D1 in Table 8 should be viewed with some caution. As noted above, the structure in the core and inner-jet regions is more complicated than that described by our three-component model. Moreover, the flux density in each unmodeled component is probably allocated differently to C1, C2, and D1 at each frequency due to differences in resolution and opacity. Nonetheless, we can still make some general comments and compare our results with previous multi-frequency studies. (1) Estimates of the spectral index of the 43 and 86 GHz identified core range between $\alpha \approx +0.6$ and $\alpha \approx -0.4$ (Gómez et al. 1999; Pagels et al. 2004; Chen et al. 2005; Krichbaum et al. 2006a). Our estimate of the spectral index of C1 between 5.0 and 8.4 GHz ($\alpha = -0.4 \pm 0.2$) is at the low end of this range, and consistent with an isolated core several months removed from its most recent ejection (Pagels et al. 2004). Our spectral-index estimate for C1 between 8.4 and 15.4 GHz ($\alpha = -0.9 \pm 0.2$) suggests that the component between C1 and C2 is contributing fractionally more flux density to C1 at 8.4 GHz than at 15.4 GHz (where it is partially resolved). (2) The "stationary" component ∼0.65 mas from the core is modeled by Chen et al. (2005) for their 1999 May epoch as a synchrotron self-absorbed source, with a turnover frequency between 5.0 and 8.4 GHz. The flat spectral index we estimate for C2 between 5.0 and 8.4 GHz ($\alpha = -0.2 \pm 0.2$) is consistent with this interpretation. Our spectral-index estimate for C2 between 8.4 and 15.4 GHz ($\alpha = -1.1 \pm 0.2$) suggests that the component west-southwest of C2 is contributing fractionally more flux density to C2 at 8.4 GHz than at 15.4 GHz. (3) Chen et al. (2005) find for a component located ∼1.5 mas west-southwest of the core a spectral index of $\alpha \approx -0.9$. Our spectral-index estimates for D1 ($\alpha \approx -1.4$ to -0.8) are roughly consistent with this value, but again suggest that components between C2 and D1 are contributing fractionally more flux density to D1 at 5.0 and 8.4 GHz than at 15.4 GHz.

In contrast to the core and inner-jet regions, the extended-jet region appears to be reasonably well represented by our two-component model at 5.0 and 8.4 GHz, and likewise the (immediate) jet-peak region by our one-component model at 15.4 GHz. Our estimates of the spectral index of J1 ($\alpha \approx -1.2$ to -1.0) are self-consistent and also consistent with the spectral index ($\alpha \approx -0.9$) estimated by Chen et al. (2005) for a component approximately ∼5.5 mas west of the core. We note that the lower-level structure extending west of J1 in the 15.4 GHz image is likely real, and not a noise spike or sidelobe of one of the bright core-region components. Its appearance is robust against changes (e.g., to the positioning of CLEAN windows) in the imaging process. The east–west extension at J1 at all three frequencies is, perhaps, a consequence of a near superposition of jet components undergoing the change in trajectory described in Section 5.2.3.

Can we determine the ejection epoch for the component seen between C1 and C2 in our 15.4 GHz image for 2004 May 18, and perhaps also the time of transit of the component from C1 to C2? Our 8.4 GHz image for 2003 September 8 shows a "sudden" brightening of C1 relative to C2 not seen 2003 May 18 or earlier. On 2003 December 5, the 8.4 GHz brightness peak is very nearly aligned with the center of C1. Over the next several epochs, the brightness peak moves westward, and by 2005 January 15 is very nearly aligned with the center of C2. If we assume that the brightening in 2003 September 8 temporally coincides (within ∼1–2 months) with the ejection of a new component from the "core," then we may interpret the subsequent shifts in the position of the brightness peak as roughly tracking the motion of the new component between the positions defined by C1 and C2. The total transit time, using 2003 September 8 as the epoch of ejection and 2005 January 15 as the epoch of arrival, is ∼1.4 yr. The 2004 May 18 epoch represents the approximate mid-point of this interval.

6. QUASAR B2250+194

6.1. VLBI Images at 8.4 GHz

We present in Figure 10 the 8.4 GHz images of B2250+194 generated from each of the 35 sessions of VLBI observations made between 1997 January and 2005 July. The image characteristics are summarized in Table 9. The images reveal a relatively compact source. Near the brightness peak, the source shows no deviation from the restoring beam, down to the ∼10% level. Below this level, i.e., at the brightness level of the outermost five or six contours, the source shows a distinct "kidney-bean" shape: The northern portion of the source bends ∼30° to the west, while the southern portion of the source bends ∼10° to the west. Other than the ∼25% increase in the peak brightness over the ∼8.5 yr period of our observing program, there is no significant indication of radio structure evolution in the images. The low-level kidney-bean structure may trace (1) continuous emission along a single, bent jet; (2) emission from well-separated regions in a single, bent jet viewed nearly straight on; or (3) emission from a pair of bent (or at least not quite counteraligned) jets. If scenario 1 is correct, then the core of the quasar could be located at either the north or south end of the source, and the centrally located brightness peak would be a bright jet component. If, however, scenario 2 or 3 is correct, then the brightness peak could be nearly aligned with the core. We elaborate more on these options in Sections 6.2 and 6.3.

6.2. u–v-plane Model Fitting at 8.4 GHz

To more quantitatively investigate changes in the radio structure of B2250+194, we fit to the *u–v* data, not including

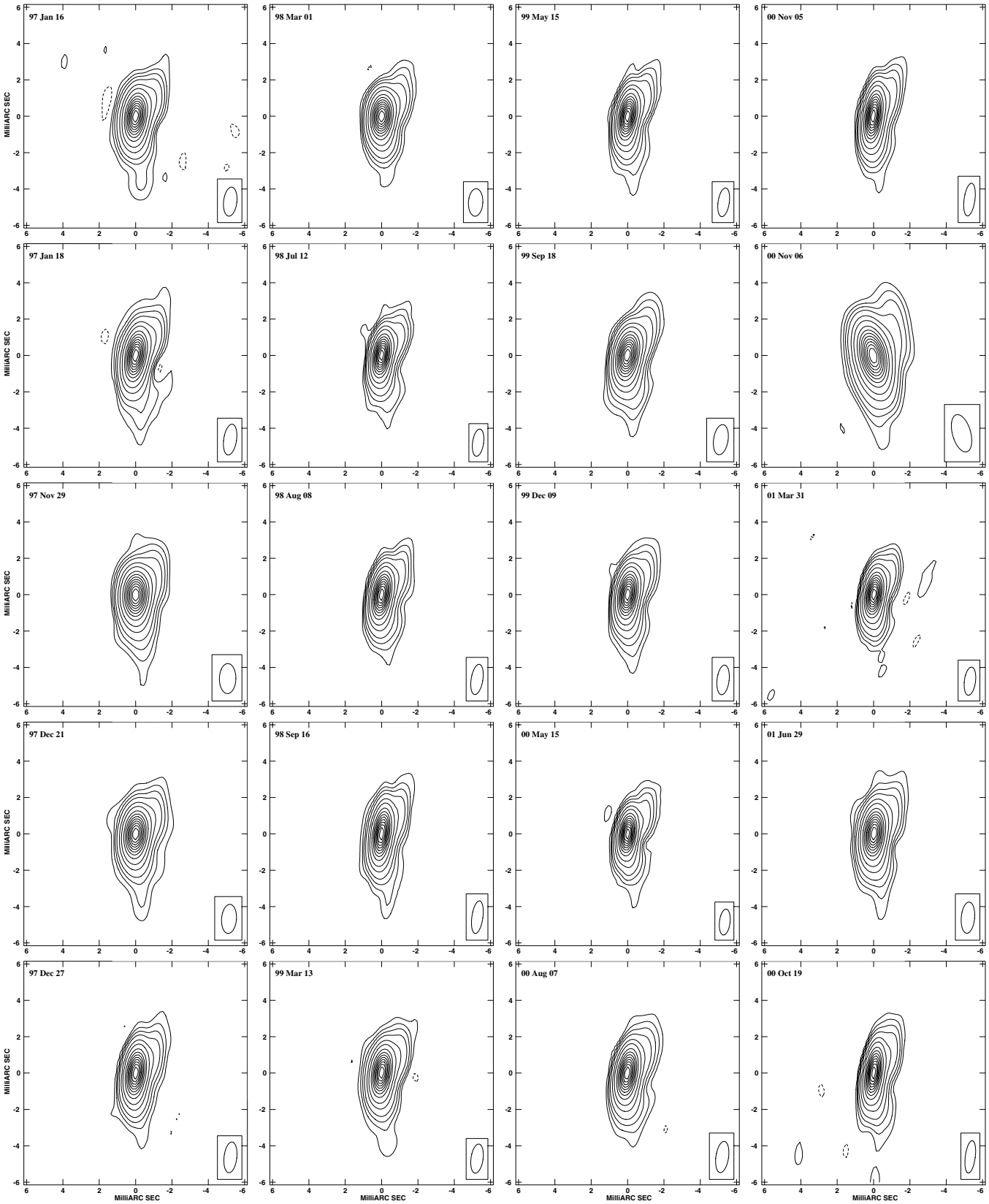

Figure 10. 8.4 GHz VLBI images of B2250+194 for each of our 35 observing sessions between 1997 January and 2005 July. In each image the contour levels are 0.2%, 0.5%, 1%, 2%, 5%, 10%, 20%, 30%, 40%, 50%, 60%, 70%, 80%, and 90% of the peak brightness. An additional contour, denoting −0.2% of the brightness peak, appears in some of the images. Image characteristics are summarized in Table 9. The restoring beam is indicated in the bottom-right-hand corner of each image. The image for each epoch is centered on the brightness peak, which is offset from the phase center (i.e., origin of coordinates) by <0.02 mas in each of α and δ.

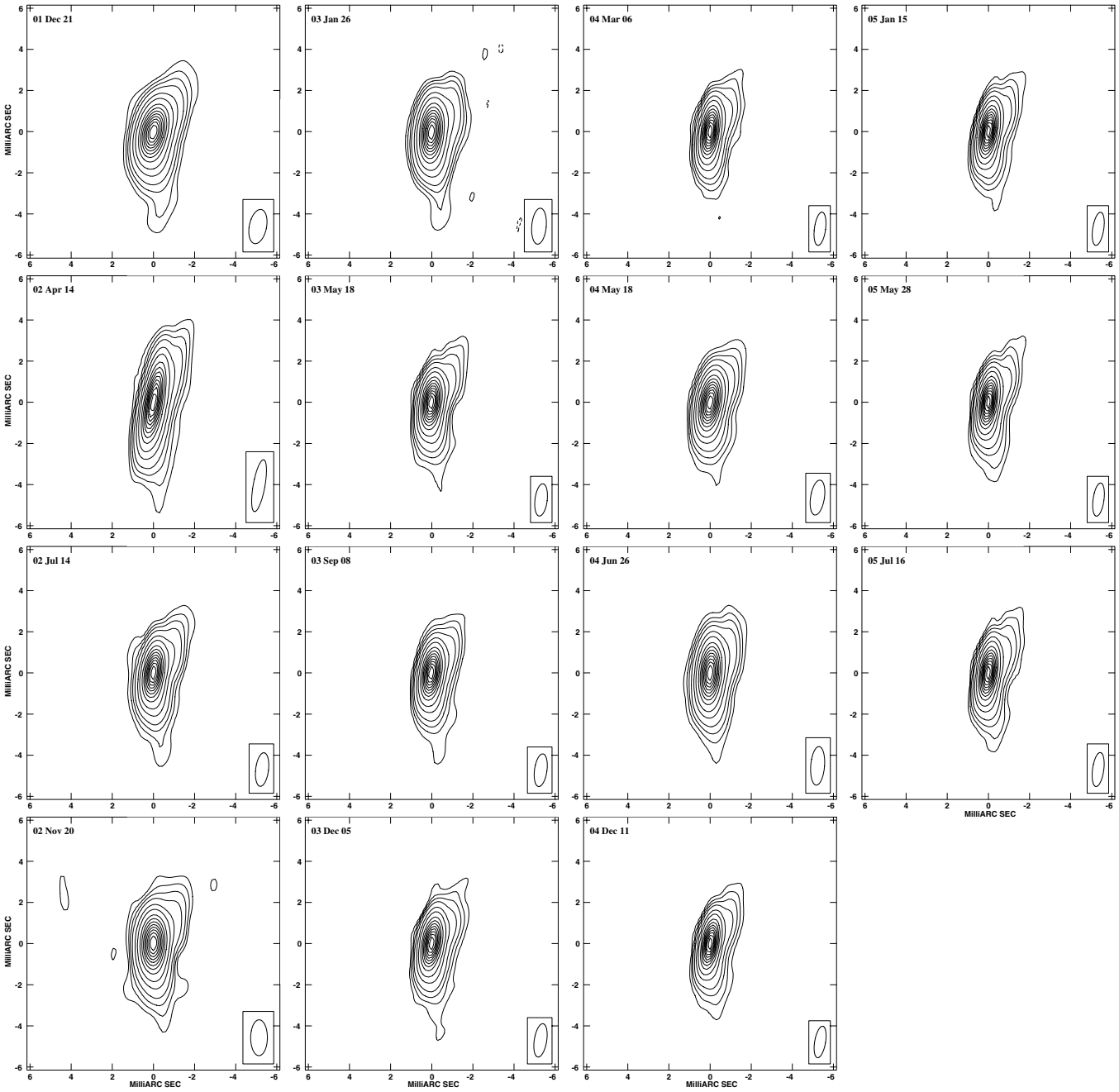

Figure 10. (Continued)

baselines to the 70 m DSN Tidbinbilla (Ti) telescope (see below), a model consisting of a single elliptical Gaussian. The results for the fits are given in Table 10 and illustrated in Figure 11. The uncertainty in each parameter at each epoch is a standard error; it includes contributions, added in quadrature, from both the statistical standard error of the fit and the systematic error associated with the particular u–v coverage. To estimate the systematic error we performed the fit at each epoch an additional five or six times, using for each additional fit only a subset (8–12 telescopes) of the full VLBI array (minus Ti). We take the systematic error for a given parameter at a given epoch to be the rms variation of the subset values about the value derived from all of the available data at that epoch. The uncertainty in the tabulated flux density at each epoch also includes the 10% standard error in the VLBI flux-density scale.

Figure 11 shows that the size of the Gaussian (parameterized by major and minor axis lengths) is variable from epoch to epoch, and that there is an anti-correlation between the size and flux density of the Gaussian. In contrast, the orientation of the Gaussian is approximately constant (P.A. of the major axis $= -11^\circ \pm 2^\circ$). While the apparently random epoch-to-epoch fluctuations in the size of the Gaussian may well be largely due to limitations of the one-component model, the anti-correlation between size and flux density suggests that activity is at least mainly confined to a relatively compact region, namely the core or a shocked region of the jet.

We did not include data from baselines to Ti in our above analysis since Ti was not used consistently over the ∼8.5 yr period of our observing program, and because including these data led to systematic variations in the results for the size

Table 9
B2250+194 Image Characteristics

Start Date	Peak ($mJy\,\Omega_b^{-1}$) [1]	Min. ($mJy\,\Omega_b^{-1}$) [2]	rms ($mJy\,\Omega_b^{-1}$) [3]	Θ_{maj} (mas) [4]	Θ_{min} (mas) [5]	P.A. (°) [6]	CLEAN (mJy) [7]	$[\frac{CLEAN}{VLA}]$ [8]
1997 Jan 16	318	−0.85	0.18	1.60	0.73	−6.39	407	0.93
1997 Jan 18	314	−0.80	0.14	1.71	0.70	−8.38	396	0.92
1997 Nov 29	356	−0.65	0.18	1.65	0.91	−0.96	415	0.89
1997 Dec 21	383	−0.63	0.14	1.60	0.82	−4.45	457	1.01
1997 Dec 27	367	−0.75	0.16	1.70	0.70	−6.38	429	0.99
1998 Mar 1	401	−0.83	0.15	1.51	0.79	−3.12	468	0.96
1998 Jul 12	360	−0.70	0.15	1.51	0.61	−8.03	435	0.97
1998 Aug 8	373	−0.64	0.12	1.68	0.64	−8.94	438	1.05
1998 Sep 16	360	−0.60	0.14	1.81	0.61	−7.84	440	0.97
1999 Mar 13	313	−0.66	0.12	1.61	0.66	−7.87	401	0.93
1999 May 15	347	−0.37	0.09	1.59	0.62	−8.41	428	0.94
1999 Sep 18	382	−0.76	0.14	1.67	0.80	−8.65	445	1.06
1999 Dec 9	360	−0.57	0.12	1.64	0.66	−6.67	433	0.93
2000 May 15	357	−0.64	0.15	1.43	0.58	−6.52	441	1.02
2000 Aug 7	346	−0.72	0.12	1.73	0.69	−8.13	412	0.98
2000 Nov 5	354	−0.41	0.10	1.81	0.59	−7.77	429	0.98
2000 Nov 6	341	−0.67	0.17	2.12	1.00	15.75	406	0.92
2001 Mar 31	331	−0.79	0.14	1.56	0.61	−7.17	403	0.91
2001 Jun 29	320	−0.59	0.08	1.72	0.74	−4.87	401	1.02
2001 Oct 19	269	−0.83	0.19	1.79	0.55	−7.32	347	0.91
2001 Dec 21	321	−0.53	0.11	1.69	0.84	−11.40	406	...
2002 Apr 14	276	−0.49	0.13	2.56	0.57	−10.13	339	0.94
2002 Jul 14	264	−0.46	0.11	1.64	0.62	−6.85	354	...
2002 Nov 20	314	−0.62	0.16	1.74	0.81	−0.34	396	...
2003 Jan 26	312	−0.71	0.17	1.75	0.70	−4.99	401	0.95
2003 May 18	330	−0.52	0.10	1.58	0.59	−6.79	409	0.96
2003 Sep 8	390	−0.61	0.12	1.60	0.60	−7.74	468	0.98
2003 Dec 5	408	−0.80	0.15	1.64	0.60	−8.95	488	...
2004 Mar 6	437	−0.55	0.13	1.63	0.54	−7.54	516	1.01
2004 May 18	456	−0.63	0.16	1.71	0.67	−8.95	529	0.99
2004 May 18(C)[a]	290	−0.70	0.18	3.04	0.96	−11.21	367	0.96
2004 May 18(U)[a]	502	−2.89	0.61	0.98	0.35	−7.72	567	1.01
2004 Jun 26	423	−0.55	0.10	1.88	0.67	−4.42	511	0.97
2004 Dec 11	418	−0.48	0.10	1.55	0.53	−9.74	494	0.97
2005 Jan 15	431	−0.54	0.08	1.63	0.54	−8.81	507	0.96
2005 May 28	421	−0.38	0.09	1.62	0.53	−7.78	495	0.99
2005 Jul 16	425	−0.45	0.09	1.67	0.55	−7.67	494	0.95

Notes. Columns 1 and 2: positive and negative extrema ($\Omega_b \equiv$ CLEAN restoring beam area); Column 3: rms background level; Columns 4–6: CLEAN restoring beam major axis (FWHM), minor axis (FWHM), and position angle (east of north); Column 7: total CLEAN flux density; Column 8: ratio of VLBI-determined (Column 7) to VLA-determined (Table 2) flux density for all epochs at which the VLA observed. The estimated standard error in the VLBI-determined flux densities is 10%.
[a] C indicates 5.0 GHz; U indicates 15.4 GHz; all other observations were at 8.4 GHz.

and orientation of the elliptical Gaussian. (Because their radio structures are extended largely east–west, the results presented for sources 3C 454.3 and B2252+172 are far less sensitive to the inclusion of the long, north–south-oriented, Ti baselines.) The major-axis length (FWHM) of the Gaussian is significantly smaller and less variable when Ti baselines are included than when they are left out: 0.47 ± 0.03 mas instead of 0.66 ± 0.06 mas (for the same epochs). This comparison suggests that the Ti baselines further constrain the compact central region. Additionally, the major axis of the Gaussian rotates when Ti baselines are included: $-11° \pm 2°$ p.a. becomes $-26° \pm 3°$. The $-26°$ estimate plausibly better represents the alignment of the jet axis near the core (see Section 6.3).

We attempted to separate the changes in the compact central region from changes in the lower-level structure to the northwest and south-southwest by also fitting to the *u*–*v* data a model consisting of three point sources. Unfortunately, we were unable to adequately separate the three components: we found the same anti-correlation between overall source size and total flux density with the three-component model as with the one-component model; i.e., we found that during periods of increased flux density (1) the flux densities of all three components increased, and (2) the northwest and southwest components moved closer to the central component (which we fixed to the position of the brightness peak at each epoch). We also found no significant change with time of the angles of the position vectors drawn from the center component to the northwest component or from the center component to the southwest component.

6.3. VLBI Images at 5.0 and 15.4 GHz

We present in Figure 12 the 5.0, 8.4, and 15.4 GHz images of B2250+194 generated for the VLBI observations on 2004 May 18. The 8.4 GHz image is the same as that presented in Figure 10 except for the omission of the lowest contour level. The image characteristics are given in Table 9.

Table 10
B2250+194 u–v-plane 8.4 GHz Model Parameters

Start Date	$S_{8.4}$ (mJy) [1]	σ_S (mJy) [2]	Maj (mas) [3]	$\sigma_{\rm Maj}$ (mas) [4]	Min (mas) [5]	$\sigma_{\rm Min}$ (mas) [6]	P.A. (°) [7]	$\sigma_{\rm P.A.}$ (°) [8]
1997 Jan 16	357	36	0.75	0.04	0.31	0.02	−10	3
1997 Jan 18	346	35	0.75	0.04	0.29	0.02	−13	3
1997 Nov 29	395	40	0.62	0.05	0.21	0.02	−10	4
1997 Dec 21	436	44	0.69	0.04	0.22	0.02	−10	3
1997 Dec 27	413	41	0.67	0.04	0.20	0.02	−10	3
1998 Mar 1	455	46	0.68	0.04	0.20	0.02	−8	2
1998 Jul 12	413	41	0.63	0.04	0.21	0.02	−11	3
1998 Aug 8	419	42	0.59	0.03	0.21	0.01	−9	3
1998 Sep 16	423	42	0.71	0.04	0.26	0.02	−8	2
1999 Mar 13	386	39	0.78	0.03	0.29	0.01	−10	2
1999 May 15	413	41	0.72	0.03	0.25	0.01	−12	2
1999 Sep 18	425	42	0.61	0.03	0.19	0.01	−16	3
1999 Dec 9	416	42	0.66	0.03	0.24	0.01	−14	2
2000 May 15	417	42	0.64	0.03	0.20	0.01	−13	2
2000 Aug 7	392	39	0.66	0.03	0.22	0.01	−12	2
2000 Nov 5	415	41	0.70	0.03	0.24	0.01	−10	2
2000 Nov 6	393	39	0.74	0.06	0.29	0.03	−5	3
2001 Mar 31	394	39	0.69	0.03	0.26	0.01	−14	2
2001 Jun 29	386	39	0.80	0.03	0.29	0.01	−10	2
2001 Oct 19	364	36	0.79	0.04	0.31	0.02	−14	4
2001 Dec 21	385	39	0.83	0.03	0.30	0.01	−15	3
2002 Apr 14	327	33	0.76	0.03	0.29	0.01	−10	3
2002 Jul 14	327	33	0.82	0.03	0.27	0.01	−10	2
2002 Nov 20	359	36	0.73	0.04	0.19	0.01	−11	2
2003 Jan 26	395	39	0.83	0.07	0.28	0.02	−9	2
2003 May 18	393	39	0.70	0.03	0.25	0.01	−11	2
2003 Sep 8	449	45	0.63	0.03	0.22	0.01	−13	2
2003 Dec 5	471	47	0.64	0.03	0.23	0.01	−12	2
2004 Mar 6	501	50	0.61	0.02	0.22	0.01	−11	2
2004 May 18	512	51	0.60	0.03	0.21	0.01	−13	3
2004 Jun 26	496	50	0.68	0.05	0.25	0.02	−9	2
2004 Dec 11	475	47	0.59	0.03	0.20	0.01	−13	2
2005 Jan 15	490	49	0.62	0.03	0.20	0.01	−12	2
2005 May 28	477	48	0.59	0.03	0.20	0.01	−10	2
2005 Jul 16	478	48	0.59	0.02	0.19	0.01	−11	2

Notes. Columns 1 and 2: integrated flux density and its standard error; Columns 3 and 4: major-axis length (FWHM) and its standard error; Columns 5 and 6: minor-axis length (FWHM) and its standard error; Columns 7 and 8: position angle (east of north) of major axis, and its standard error. The tabulated flux-density standard errors include the estimated 10% standard error in the VLBI flux-density scale at each epoch.

The images at all three frequencies show a compact emission region near the brightness peak and low-level emission to the northwest and south or south-southwest. The upper limit on the angular size of the compact emission region is set approximately by the angular resolution of our VLBI array at 15.4 GHz (see below). Between 5.0 and 15.4 GHz, the peak flux density in the images increases ∼73%, and the total CLEAN flux density increases ∼55%. When taken together with our observation that the flux density at 8.4 GHz is at or near a maximum on 2004 May 18 (see top panel in Figure 11), the small size and inverted spectrum (between 5.0 and 15.4 GHz) of the compact central region suggest that the brightness peak in the image at each frequency nearly coincides with the core. Scenario 1 above (see Section 6.1), which places the core at either the north or south end of the source, thus seems unlikely.

We fit to the 5.0 and 15.4 GHz u–v data the same one-component model described in Section 6.2. The results are given in Table 11. The uncertainties are standard errors (see Section 6.2), with the flux-density uncertainties including also a 5% uncertainty in the VLBI flux-density scale for 2004 May 18. We adopt a (conservative) 5% uncertainty for this epoch rather than the nominal 10% (see Section 4.3), because the VLBI- and VLA-determined flux densities at each frequency differ by only 1%–4% (see Table 9). The results at each frequency for the flux density, size, and orientation of the Gaussian are consistent with a compact emission region near the brightness peak that is progressively more dominant, relative to the surrounding low-level emission, as the frequency increases from 5.0 to 15.4 GHz. We estimate, using the 3σ upper limit on the major-axis length (FWHM) of the Gaussian at 15.4 GHz, a maximum diameter for the compact emission region of 0.40 mas. The orientation of the Gaussian at 15.4 GHz (p.a. $= -25^\circ \pm 4^\circ$) is consistent with that at 8.4 GHz when Ti baselines are included in the fit. This consistency supports the accuracy of the results obtained by including Ti baselines at 8.4 GHz, and provides additional evidence for the underlying orientation of the jet axis near the core. (Note that telescope Ti did not observe at either 5.0 or 15.4 GHz.) The decrease in the spectral index from $\alpha = 0.79 \pm 0.15$ between 5.0 and 8.4 GHz to $\alpha = 0.12 \pm 0.13$ between 8.4 and 15.4 GHz is consistent with the spectrum for the compact emission region peaking at a frequency near 15.4 GHz.

Table 11
B2250+194 u–v-plane Model Parameters for 2004 May 18

ν (GHz)	S_ν (mJy) [1]	σ_S (mJy) [2]	Maj (mas) [3]	$\sigma_{\rm Maj}$ (mas) [4]	Min (mas) [5]	$\sigma_{\rm Min}$ (mas) [6]	P.A. (°) [7]	$\sigma_{\rm P.A.}$ (°) [8]
5.0	342	19	0.81	0.13	0.51	0.02	−15	5
8.4	512	27	0.60	0.03	0.21	0.01	−13	3
15.4	549	32	0.31	0.03	0.12	0.02	−25	4

Notes. Columns 1 and 2: integrated flux density and its standard error; Columns 3 and 4: major-axis length (FWHM) and its standard error; Columns 5 and 6: minor-axis length (FWHM) and its standard error; Columns 7 and 8: position angle (east of north) of major axis, and its standard error. The tabulated flux-density standard errors include the estimated 5% standard error in the VLBI flux-density scale for 2004 May 18.

7. RADIO SOURCE B2252+172

7.1. VLBI Images at 8.4 GHz

We present in Figure 13 the 8.4 GHz images of B2252+172 generated from each of the 12 sessions of VLBI observations made between 2002 November and 2005 July. The image characteristics are summarized in Table 12. The images reveal a source consisting of a relatively bright, compact emission region and extended emission at or just above the noise level. Near the brightness peak, the source shows no deviation from the restoring beam, down to the ∼10% level. Below this level, i.e., at the brightness level of the outermost three or four contours, the source extends west of the brightness peak. For our last three epochs, a very weak emission component, itself extended east–west, appears (above the new peaks in the background) ∼2.6 mas west-southwest of the brightness peak. This component is likely real, since its appearance is robust for these epochs against changes (e.g., to the positioning of CLEAN windows) in the imaging process. The flux density of this component is ∼0.7 mJy. Variations in the quality of the images

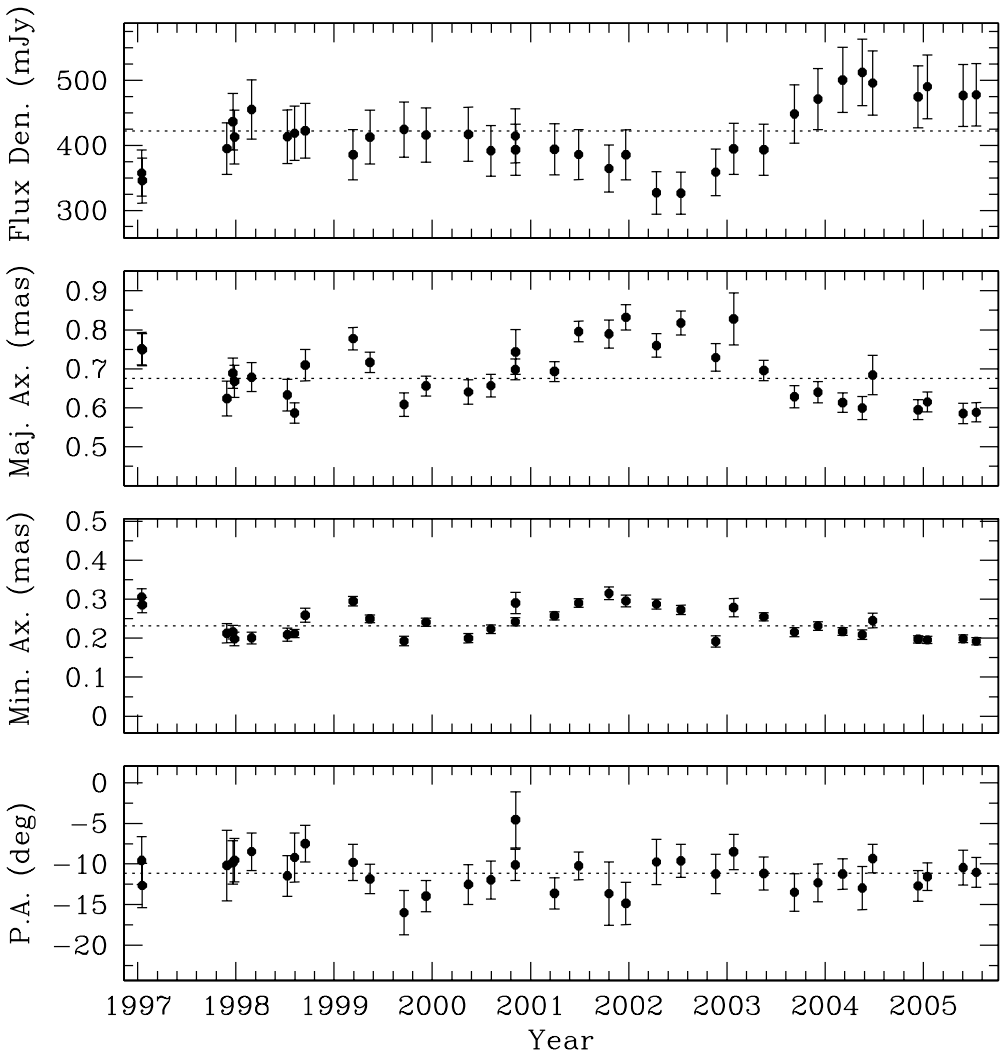

Figure 11. B2250+194 model parameters (see also Table 10). Panels, top to bottom, are integrated flux density, major-axis length (FWHM), minor-axis length (FWHM), and position angle (east of north) of the major axis. Error bars represent the standard errors in the estimates of the corresponding parameter. The dotted line in each panel represents the weighted mean of the parameter value over the 35 epochs.

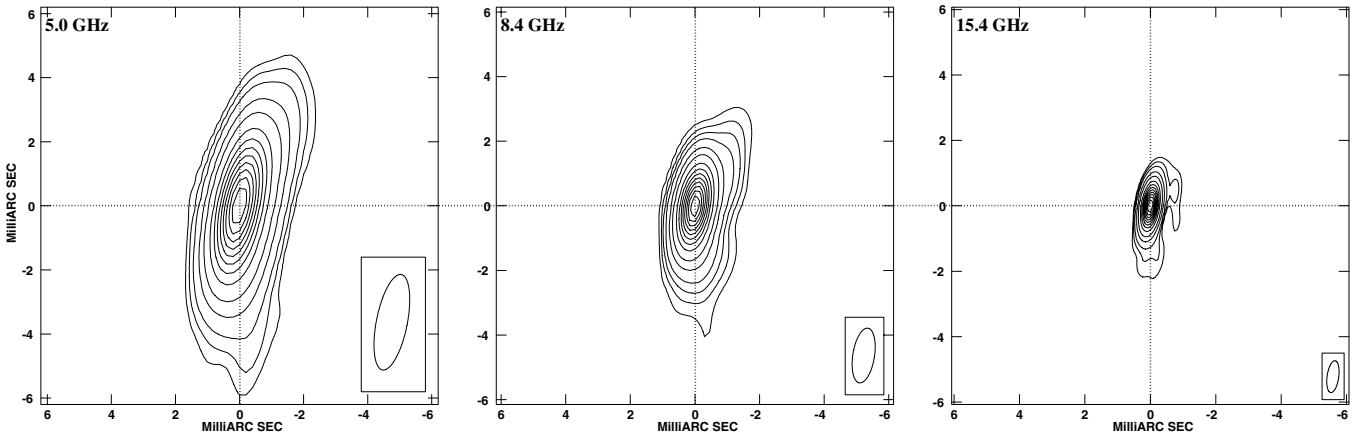

Figure 12. 5.0, 8.4, and 15.4 GHz VLBI images of B2250+194 for epoch 2004 May 18. Contour levels are 0.5%, 1%, 2%, 5%, 10%, 20%, 30%, 40%, 50%, 60%, 70%, 80%, and 90% of the peak brightness in each image. Image characteristics are summarized in Table 9. The restoring beam is indicated in the bottom right-hand corner of each image. The images are centered, as indicated by the dotted lines, on the brightness peak in each image.

from epoch to epoch[11] make it difficult to trace any motion of this component relative to the brightness peak. However, there is evidence for the evolution of the low-level emission ∼0.5 mas to ∼1.5 mas west of the brightness peak. The peak flux density in the image for 2003 May is at or near the maximum we observed during the ∼2.7 yr span of our observations of this source. The low-level emission at this 2003 May epoch shows

[11] The quality of the image for B2252+172 for a given epoch is a function of the accuracy of the phase referencing, as well as the brightness distribution and flux density of the source (see Section 4.1).

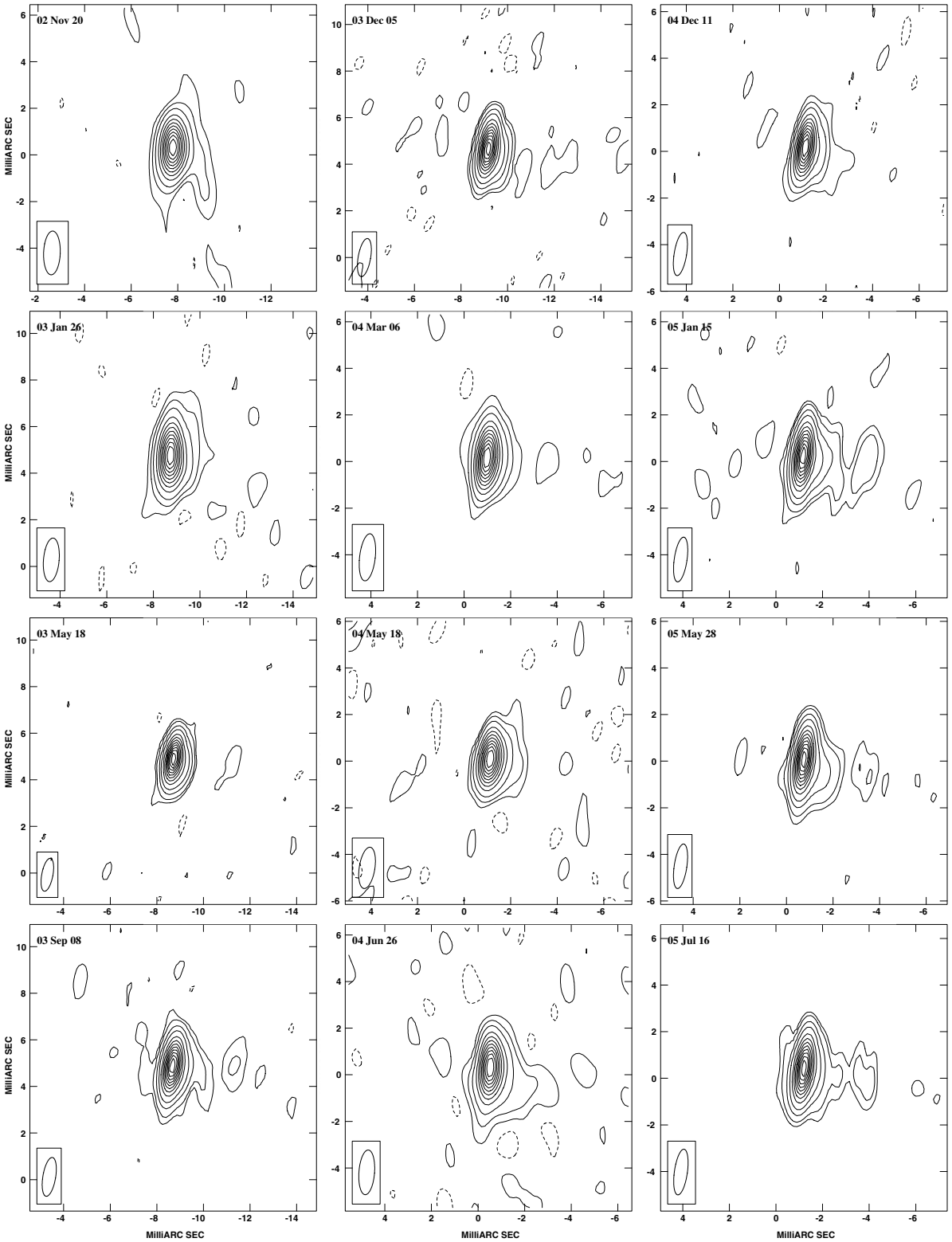

Figure 13. 8.4 GHz VLBI images of B2252+172 for each of the 12 observing sessions between 2002 November and 2005 July. The lowest contour level in each image is chosen to display some noise, and is either ±1% or ±2% of the peak brightness in the image. In images where the lowest contour is ±1%, the 2% contour is also shown. The remaining contour levels in each image are 5%, 10%, 20%, 30%, 40%, 50%, 60%, 70%, 80%, and 90% of the peak brightness in the image. Image characteristics are summarized in Table 12. The restoring beam is indicated in the bottom left-hand corner of each image. The image for each epoch is centered on the brightness peak. The up to ∼10 mas offset in each image between the position of the brightness peak and the phase center (i.e., origin of coordinates) largely reflects inaccuracies in the assumed positions of B2252+172 and (phase reference source) 3C 454.3 used at the correlator.

minimal separation from the brightness peak. In subsequent epochs, the low-level emission extends increasingly westward toward the ∼0.7 mJy component. This evolution is consistent with the ejection and subsequent motion of a new jet component. The brightness peak in each image near the easternmost edge of the source and the apparent westward motion of the low-level

Table 12
B2252+172 Image Characteristics

Start Date	Peak ($mJy\,\Omega_b^{-1}$) [1]	Min. ($mJy\,\Omega_b^{-1}$) [2]	rms ($mJy\,\Omega_b^{-1}$) [3]	Θ_{maj} (mas) [4]	Θ_{min} (mas) [5]	P.A. (°) [6]	CLEAN (mJy) [7]	$[\frac{CLEAN}{VLA}]$ [8]
2002 Nov 20	14.5	−0.41	0.10	1.88	0.71	−2.14	18.0	...
2003 Jan 26	14.3	−0.65	0.12	1.88	0.67	−4.93	20.6	0.82
2003 May 18	18.7	−0.34	0.08	1.44	0.48	−10.68	22.9	0.85
2003 Sep 8	15.9	−0.28	0.06	1.69	0.55	−9.40	18.7	0.87
2003 Dec 5	16.4	−0.34	0.08	1.66	0.53	−9.84	19.1	...
2004 Mar 6	12.4	−0.37	0.08	2.03	0.67	−6.62	15.2	0.89
2004 May 18	9.7	−0.51	0.15	1.79	0.67	−8.85	12.5	0.78
2004 May 18(C)[a]	10.2	−0.56	0.17	3.20	0.95	−10.96	14.3	0.83
2004 May 18(U)[a]	9.3	−2.31	0.60	1.16	0.59	9.62	10.2	0.89
2004 Jun 26	8.9	−0.36	0.10	1.92	0.67	−4.22	13.0	0.82
2004 Dec 11	11.6	−0.39	0.09	1.87	0.53	−9.14	15.5	0.85
2005 Jan 15	11.6	−0.16	0.05	1.94	0.55	−8.26	15.4	0.88
2005 May 28	16.8	−0.19	0.05	1.93	0.54	−8.30	20.8	0.90
2005 Jul 16	16.9	−0.18	0.04	1.98	0.56	−7.98	21.0	0.80

Notes. Columns 1 and 2: positive and negative extrema ($\Omega_b \equiv$ CLEAN restoring beam area); Column 3: rms background level; Columns 4–6: CLEAN restoring beam major axis (FWHM), minor axis (FWHM), and position angle (east of north); Column 7: total CLEAN flux density; Column 8: ratio of VLBI-determined (Column 7) to VLA-determined (Table 2) flux density for all epochs at which the VLA observed. The flux-density ratios (Column 8) indicate that the CLEAN components do not contain all the flux density from the low-level emission. The estimated standard error in the VLBI-determined peak flux densities is 10%.
[a] C indicates 5.0 GHz; U indicates 15.4 GHz; all other observations were at 8.4 GHz.

emission suggests that the brightness peak nearly coincides with the core.

7.2. *u–v*-plane Model Fitting at 8.4 GHz

To more quantitatively investigate changes in the radio structure of B2252+172 near its brightness peak, we fit to the *u–v* data a model consisting of a single elliptical Gaussian. Our results (not tabulated) show that the emission region near the brightness peak is elongated along P.A. $= 73° \pm 8°$ and has a major-axis length (FWHM) of 0.35 ± 0.07 mas. The quoted parameter values and uncertainties are the mean and rms variation about the mean over our 12 observing sessions. The orientation of the Gaussian suggests that the jet axis may bend slightly from P.A. $\sim 73°$ near the position of the brightness peak to P.A. $\sim 90°$ at distances $\gtrsim$1 mas from the brightness peak (see also Figure 13). No systematic variations in either the orientation or the size of the Gaussian are evident over our 12 epochs.

We also fit to the data a two-point-source model in an attempt to characterize the changes observed in the low-level emission immediately west of the brightness peak. Unfortunately, the S/N of the phase-referenced data was not sufficiently high to adequately constrain both the relatively bright component near the brightness peak and the weak secondary component.

7.3. VLBI Images at 5.0 and 15.4 GHz

We present in Figure 14 the 5.0, 8.4, and 15.4 GHz images of B2252+172 generated for the VLBI observations on 2004 May 18. The 8.4 GHz image is the same as that presented in Figure 13 except for the omission of the lowest contour level. The image characteristics are given in Table 12.

The images at 5.0 and 8.4 GHz each show a compact emission region near the brightness peak and low-level emission to its west. The image at 15.4 GHz shows that the compact emission region is marginally extended northeast–southwest. The component ∼2.6 mas west-southwest of the brightness peak, identified in the 8.4 GHz images only at later epochs, already appears prominently in the 5.0 GHz image for 2004 May 18. The greater prominence at 5.0 GHz of this component is consistent with steep-spectral-index emission from one or more jet components perhaps several years after ejection. The evolving low-level emission observed at 8.4 GHz closer to the brightness peak (see Section 7.1) may derive from a more recent ejection event.

We fit to the 5.0 and 15.4 GHz *u–v* data the same one-component model described in Section 7.2. At 5.0 GHz, the best-fit Gaussian is elongated along P.A. $= 67° \pm 11°$ and has major-axis length (FWHM) 0.57 ± 0.09 mas. At 15.4 GHz, the Gaussian is elongated along P.A. $= 70° \pm 6°$ and has major-axis length (FWHM) 0.33 ± 0.04 mas. The uncertainties are standard errors, for which the systematic contributions were estimated using a procedure similar to that described in Section 6.2. The results for the orientation are consistent with the mean value (P.A. $= 73° \pm 8°$) found at 8.4 GHz for the 12 epochs we observed this source. Using the 3σ upper limit on the major-axis length (FWHM) of the Gaussian at 15.4 GHz, we estimate a maximum diameter of 0.45 mas for the compact emission region about the brightness peak. The flat spectrum of the emission between 5.0 and 15.4 GHz ($\alpha = -0.17 \pm 0.07$) suggests that the brightness peak in the image at each frequency nearly coincides with the core.

8. DISCUSSION

8.1. The 8.4 GHz Core of Quasar 3C 454.3

Our 35 images at 8.4 GHz, obtained from data gathered between 1997 January and 2005 July, show that the core region (easternmost ∼1 mas) of 3C 454.3 is quite variable. For each epoch, we fit to the core region in the image a model consisting of two point sources. We refer to the eastern component as C1 and the western component as C2. Our 8.4 GHz two-component model only approximately represents the complex underlying structure seen in VLBI images at higher frequencies (namely 43 GHz and 86 GHz). Nevertheless, we determined via a simulation study that C1 and C2 are closely aligned with

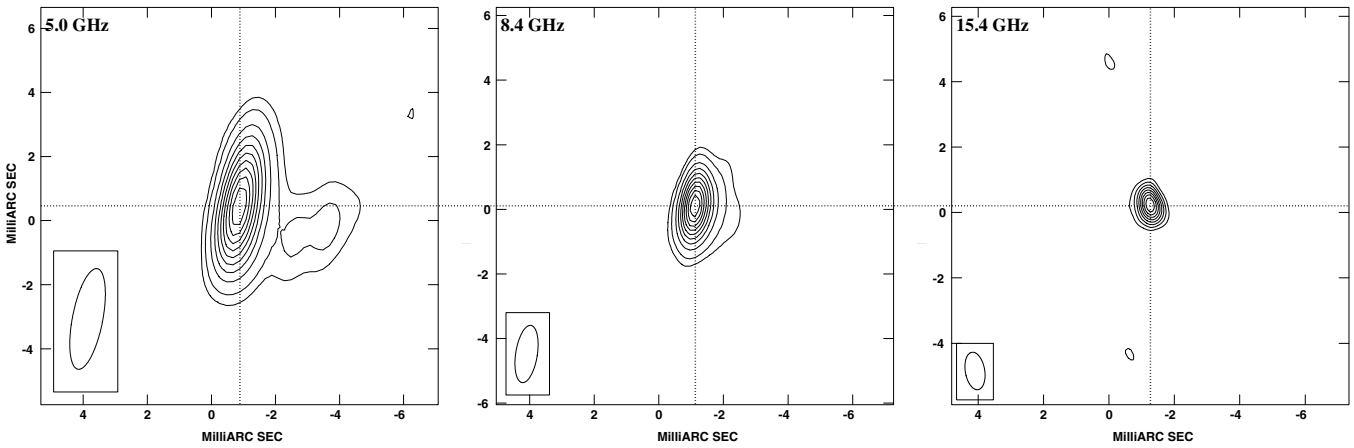

Figure 14. 5.0, 8.4, and 15.4 GHz VLBI images of B2252+172 for epoch 2004 May 18. Contour levels in the 5.0 and 8.4 GHz images are 0.5%, 1%, 2%, 5%, 10%, 20%, 30%, 40%, 50%, 60%, 70%, 80%, and 90% of the peak brightness in each image. Contour levels in the 15.4 GHz image are 20%, 30%, 40%, 50%, 60%, 70%, 80%, and 90% of the peak brightness in the image. Image characteristics are summarized in Table 12. The restoring beam is indicated in the bottom-left-hand corner of each image. The images are centered, as indicated by the dotted lines, on the brightness peak in each image.

the two principal 43 GHz components identified by Jorstad et al. (2001, 2005): C1 is located 0.18 ± 0.06 mas west of the 43 GHz core and C2 is located 0.06 ± 0.08 mas west-southwest of the "stationary" component located ~0.65 mas west of the 43 GHz core. Since component C1 is the more nearly aligned with the 43 GHz core, we consider it to be the 8.4 GHz core. The uncertainties quoted above represent real variations in the positions of C1 and C2, which appear to be largely caused by the westward motion of new components along the jet axis. The 43 GHz images of Jorstad et al. (2001, 2005) show the passage of four new jet components between the core and "stationary" component between 1997 January and 2001 March (the time period in common between our and Jorstad et al.'s VLBI programs). If we consider a simplified picture for the core region consisting of the core, new jet component, and the "stationary" component, then we can interpret the position changes of C1 and C2 as follows: After its ejection, the jet component moves west away from the core. Since the 8.4 GHz images do not resolve the core and jet component, C1 shifts first slightly west. As the jet component continues westward, separating itself further from the core, C1 eventually "relaxes" back east toward the core. The 0.06 mas value of the rms scatter suggests that the forward-and-back "motion" of C1 spans not much more than 0.12 mas. A similar scenario occurs as the jet component approaches and subsequently passes the "stationary" component. Here, C2 shifts first east, then west, and finally back to its starting point. The rms scatter (0.08 mas) suggests that the back-forward-back "motion" of C2 spans not much more than 0.16 mas.

The proper motion of C2 with respect to C1 between 1997 January and 2005 July was -0.034 ± 0.004 mas yr^{-1} in α and -0.014 ± 0.004 mas yr^{-1} in δ. This relative proper motion corresponds to an apparent transverse velocity of $\sim 0.9\,c$ (see Figure 15). This result indicates that over the ~8.5 yr period of our observing program either C1 "moved" systematically east-northeast and/or C2 "moved" systematically west-southwest. Given the proximity of C1 to the 43 GHz core, the latter is more likely. Moreover, VLBI images at 43 and 86 GHz produced from observations between 2005 July and November (Krichbaum et al. 2006a; Jorstad et al. 2010) show the presence of a bright, extended jet component with peak ~0.4 mas west of the "stationary" component. A plausible westward motion of this component at earlier epochs, first toward,

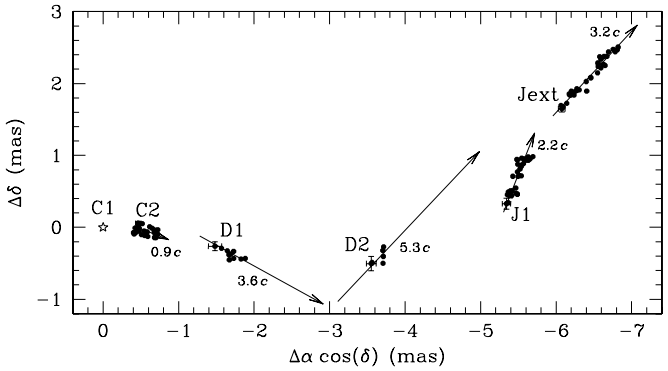

Figure 15. Two-dimensional motions of 3C 454.3 model components C2, D1, D2, J1, and Jext relative to the 8.4 GHz core (C1). The black dots are the relative position determinations at each epoch, and correspond to those plotted separately in α and δ in Figure 4 (C2), Figure 6 (D1 and D2), and Figure 7 (J1 and Jext). The first dot in the sequence for each component is accompanied by an error bar which reflects the standard error in the relative position determination. The arrows and quoted values indicate mean transverse velocity between 1997 January and 2005 July for the estimated distance of 1610 Mpc (see Paper III).

and then beyond, the nominal position of the "stationary" component, would have caused our C2 to "move" approximately westward away from C1 as we observed. The various component models of 3C 454.3 for the time period of our VLBI program appear to be able to accommodate all of the features and changes we observed at 8.4 GHz in the core region of this source.

Based on its position near the easternmost edge of the 8.4 GHz radio structure, close spatial association with the 43 GHz core, and relatively flat spectrum, we believe C1 is the best choice for the ultimate reference point for the *GP-B* guide star. The general westward motion away from C1 of the other 8.4 GHz components (see Figure 15) further supports this choice. In Paper III, we estimate the proper motion of C1 relative to the updated CRF.

8.2. Motion along the Jet Axis of Quasar 3C 454.3

We can trace in our 8.4 GHz images the motions of several jet components at varying distances from C1. We determined the proper motions (relative to C1) of D1, D2, and J1, respectively located ~1.7, ~3.7, and ~5.5 mas west of the core. The proper motion of D1 was 0.14 ± 0.02 mas yr^{-1} ($\sim 4\,c$) directed

west-southwest, and that of D2 was 0.21 ± 0.06 mas yr^{-1} ($\sim 5\,c$) directed northwest (see Figure 15). The difference in direction is consistent with the jet having a bend at a distance from the core of $\sim$3 mas.

The proper motion of J1 (see Figure 15) changed from a northwestward 0.13 ± 0.01 mas yr^{-1} ($\sim 3\,c$) between 1997 January and 2003 May to a westward 0.03 ± 0.01 mas yr^{-1} ($\sim 0.8\,c$) between 2003 September and 2005 July. The change in direction and magnitude of the proper motion of J1 may signify a second bend in the jet axis, and possibly a transition away from the highly collimated flow seen in the easternmost $\sim$5.5 mas. We observed "bulk motion" (0.13 ± 0.01 mas yr^{-1} directed northwest, see Figure 15) in the low-surface-brightness emission beyond J1, but did not identify individual components in this extended region.

8.3. Proper Motion of the Brightness Peak of Quasar B2250+194?

Our 35 images at 8.4 GHz of B2250+194 reveal a source consisting of a bright, compact emission region and low-level emission which extends both northwest and south-southwest of the brightness peak. We were unable using a three-component model to discern any relative motions in the radio structure. However, we determined using a model consisting of a single elliptical Gaussian that the size and flux density of this source were anti-correlated over the course of our observing program. This result indicates that the compact central region was likely more dominant during periods of increased flux density. By also fitting the elliptical Gaussian model to our 5.0 and 15.4 GHz data separately for 2004 May 18, we determined that near a flux-density maximum the compact central region (1) had an inverted spectrum, (2) had a diameter (at 15.4 GHz) $<$0.40 mas, and (3) was elongated (at 15.4 GHz) along P.A $\sim -25^\circ$. The brightness peak in the image for 2004 May 18 for each frequency likely nearly coincides with the core. If periodic flux density increases were accompanied by the ejection and subsequent motion of new components, then we may expect the 8.4 GHz brightness peak to have shifted approximately north-northwest or south-southeast on the sky between each flux-density maximum and the subsequent minimum. Since the overall 8.4 GHz structure of B2250+194 appears approximately static over the course of our observing program, it is likely that any shifts in the position of the brightness peak were small (peak-to-peak variations $\lesssim$0.2 mas). In Paper III, we bound the proper motion of the 8.4 GHz brightness peak of B2250+194 relative to the updated CRF.

8.4. Proper Motion of the Brightness Peak of Quasar B2252+172?

Our 12 images at 8.4 GHz of B2252+172 reveal a source consisting of a relatively bright, compact emission region and low-level emission which extends west-southwest at least $\sim$2.6 mas from the brightness peak. Using a model consisting of a single elliptical Gaussian, we determined that the compact emission region was elongated along P.A. $= 73^\circ \pm 8^\circ$ and had a diameter 0.35 ± 0.7 mas (FWHM). By also fitting the elliptical Gaussian model to our 5.0 and 15.4 GHz data separately for 2004 May 18, we determined that (at this epoch) the spectrum of the compact emission region between these frequencies was nearly flat. The brightness peak in the image for 2004 May 18 for each frequency likely nearly coincides with the core. Given the observed evolution of the low-level emission immediately west of the compact emission region, we may expect the 8.4 GHz brightness peak to have shifted slightly westward between 2002 November and 2005 July, as a possible new component was first ejected (on or near 2003 May) and then moved away from the core. Any such shift was likely small (peak-to-peak variations $\lesssim$0.2 mas), since the low-level emission is $\lesssim$10% of the brightness peak in the 8.4 GHz images. In Paper III, we bound the proper motion of the 8.4 GHz brightness peak of B2252+172 relative to the updated CRF.

9. CONCLUSIONS

Here, we give a summary of our results and conclusions (all quoted uncertainties are estimated standard errors, including allowance for systematic errors).

1. Each of our 8.4 GHz images of quasar 3C 454.3, obtained from data at 35 epochs spread between 1997 January and 2005 July, shows a bright, relatively compact core region and a bent milliarcsecond-scale jet. The images reveal significant structural changes in the core region (easternmost $\sim$1 mas), and three compact, moving jet components at various distances from the core.
2. We modeled the structure of the 3C 454.3 core region with two point sources oriented approximately east–west. We refer to the eastern component as C1 and the western component as C2. We determined a relative proper motion for C2 with respect to C1 of -0.034 ± 0.004 mas yr^{-1} in α and -0.014 ± 0.004 mas yr^{-1} in δ, an apparent transverse velocity of $\sim 0.9\,c$.
3. C1 and C2 are closely aligned with the two principal core-region components identified in VLBI images at 43 GHz by Jorstad et al. (2001, 2005): C1 is located 0.18 ± 0.06 mas west of the 43 GHz core and C2 is located 0.06 ± 0.08 mas west-southwest of a component observed at 43 GHz to be located $\sim$0.65 mas west of the core. Since component C1 is most nearly aligned with the 43 GHz core, we consider it to be the 8.4 GHz core. The "oscillations" we observed in the 8.4 GHz separation of C2 relative to C1 probably reflect the motions of new jet components periodically ejected from near the position of the 43 GHz core. The proper motion of C2 relative to C1 could be a consequence of the westward motion of a bright jet component, which was visible at the westernmost edge of the core region in 43 and 86 GHz images made one to four months after our last observing session.
4. We determined the proper motions relative to C1 of the 3C 454.3 jet components D1, D2, and J1, respectively located $\sim$1.7, $\sim$3.7, and $\sim$5.5 mas west of the core. The proper motion of D1 was 0.14 ± 0.02 mas yr^{-1} ($\sim 4\,c$) toward the west-southwest, and that of D2 was 0.21 ± 0.06 mas yr^{-1} ($\sim 5\,c$) toward the northwest. The change in the direction presumably demonstrates a bend in the jet axis $\sim$3 mas from the core. The proper motion of J1 changed from a northwestward 0.13 ± 0.01 mas yr^{-1} ($\sim 3\,c$) between 1997 January and 2003 May to a westward 0.08 ± 0.01 mas yr^{-1} ($\sim 0.8\,c$) between 2003 September and 2005 July. The change in direction and magnitude of the proper motion of J1 may signify a second bend in the jet axis $\sim$5.5 mas from the core. We observed "bulk motion" (0.13 ± 0.01 mas yr^{-1} directed northwest) in the low-surface-brightness emission beyond J1.
5. Our 15.4 GHz image of 3C 454.3 for 2004 May 18 shows a "new" jet component between C1 and C2. Our 8.4 GHz

images suggest that this component was ejected from near the position of C1 on or about 2003 September and arrived near the position of C2 ∼ 1.4 yr later.

6. Each of our 35 8.4 GHz images of quasar B2250+194 shows a bright, compact emission region and low-level emission which extends slightly, both northwest and south-southwest of the brightness peak.
7. We fit an elliptical Gaussian to the radio structure of B2250+194. We found the size and flux density of the Gaussian to be anti-correlated, suggesting that the variability of the source was greatest near the brightness peak.
8. The 8.4 GHz flux density of B2250+194 reached a maximum in our observations on or about 2004 May. Our 5.0, 8.4, and 15.4 GHz elliptical-Gaussian models for 2004 May 18 show that the compact central region (1) had an inverted spectrum, (2) had a diameter (at 15.4 GHz) <0.40 mas, and (3) was elongated (at 15.4 GHz) along P.A. $\sim -25^\circ$. The brightness peak in the image for 2004 May 18 for each frequency likely nearly coincides with the core.
9. Each of our 12 8.4 GHz images of B2252+172 shows a relatively bright, compact emission region and low-level emission which extends west-southwest at least ∼2.6 mas from the brightness peak.
10. We fit an elliptical Gaussian to the radio structure of B2252+172 and found the Gaussian to be elongated along p.a. $= 73^\circ \pm 8^\circ$ and to have a diameter 0.35 ± 0.7 mas (FWHM). Our 5.0, 8.4, and 15.4 GHz elliptical-Gaussian models for 2004 May 18 show that the compact emission region had a flat spectrum. The brightness peak in the image for 2004 May 18 for each frequency likely nearly coincides with the core.
11. Based primarily on its close spatial association with the 43 GHz core, we believe 3C 454.3 component C1 to be the best choice for the ultimate reference point for the *GP-B* guide star. The inverted to flat spectra and small bounds for any changes near their brightness peaks make B2250+194 and B2252+172 useful secondary reference sources.

We thank the anonymous referee for a constructive review of the paper and for comments helpful in the preparation of the final manuscript. This research was primarily supported by NASA, through a contract with Stanford University to the Smithsonian Astrophysical Observatory (SAO), and a subcontract from SAO to York University. The VLBA is an instrument of the NRAO, a facility of the National Science Foundation operated under cooperative agreement by Associated Universities, Inc. The DSN is operated by JPL/Caltech, under contract with NASA. We thank S. G. Jorstad for providing the 43 GHz models used in the simulation study of 3C 454.3. We have made use of the United States Naval Observatory (USNO) Radio Reference Frame Image Database (RRFID) and NASA's Astrophysics Data System Abstract Service, developed and maintained by SAO.

REFERENCES

Baars, J. W. M., Genzel, R., Pauliny-Toth, I. I. K., & Witzel, A. 1977, A&A, 61, 99
Bartel, N., Bietenholz, M. F., Lebach, D. E., et al. 2012, ApJS, 201, 3 (Paper III)
Bartel, N., Herring, T. A., Ratner, M. I., Shapiro, I. I., & Corey, B. E. 1986, Nature, 319, 733
Beasley, A. J., & Conway, J. E. 1995, in ASP Conf. Ser. 82, Very Long Baseline Interferometry and the VLBA, ed. J. A. Zensus, P. J. Diamond, & P. J. Napier (San Francisco, CA: ASP), 327
Beasley, A. J., Gordon, D., Peck, A. B., et al. 2002, ApJS, 141, 13
Bietenholz, M. F., Bartel, N., Lebach, D. E., et al. 2012, ApJS, 201, 7 (Paper VII)
Bondi, M., Padrielli, L., Fanti, R., et al. 1996, A&A, 308, 415
Briggs, D. S. 1995, BAAS, 27, 1444
Briggs, D. S., Schwab, F. R., & Sramek, R. A. 1999, in ASP Conf. Ser. 180, Synthesis Imaging in Radio Astronomy II, ed. G. B. Taylor, C. L. Carilli, & R. A. Perley (San Francisco, CA: ASP), 127
Cawthorne, T. V., & Gabuzda, D. C. 1996, MNRAS, 278, 861
Chen, T., Wardle, J. F. C., Roberts, D. H., Cheung, C. C., & Moellenbrock, G. A. 2005, in ASP Conf. Ser. 340, Future Directions in High Resolution Astronomy, ed. J. Romney & M. Reid (San Francisco, CA: ASP), 77
Cheung, C. C., Wardle, J. F. C., & Chen, T. 2005, ApJ, 628, 104
Clark, B. G. 1980, A&A, 89, 377
Condon, J. J., Cotton, W. D., Greisen, E. W., et al. 1998, AJ, 115, 1693
Cornwell, T., Braun, R., & Briggs, D. S. 1999, in ASP Conf. Ser. 180, Synthesis Imaging in Radio Astronomy II, ed. G. B. Taylor, C. L. Carilli, & R. A. Perley (San Francisco, CA: ASP), 151
Cornwell, T., & Fomalont, E. B. 1999, in ASP Conf. Ser. 180, Synthesis Imaging in Radio Astronomy II, ed. G. B. Taylor, C. L. Carilli, & R. A. Perley (San Francisco, CA: ASP), 187
Fey, A. L., Ma, C., Arias, E. F., et al. 2004, AJ, 127, 3587
Gómez, J.-L., Marscher, A. P., & Alberdi, A. 1999, ApJ, 522, 74
Jorstad, S. G., Marscher, A. P., Larionov, V. M., et al. 2010, ApJ, 715, 362
Jorstad, S. G., Marscher, A. P., Lister, M. L., et al. 2005, AJ, 130, 1418
Jorstad, S. G., Marscher, A. P., Mattox, J. R., et al. 2001, ApJS, 134, 181
Kellermann, K. I., Vermeulen, R. C., Zensus, J. A., & Cohen, M. H. 1998, AJ, 115, 1295
Kemball, A. J., Diamond, P. J., & Pauliny-Toth, I. I. K. 1996, ApJ, 464, L55
Krichbaum, T. P., Agudo, I., Bach, U., Witzel, A., & Zensus, J. A. 2006a, in Proc. of 8th European VLBI Network Symposium, ed. M. Andrzej et al. (PoS; Trieste: SISSA)
Krichbaum, T. P., et al. 2006b, in Exploring the Cosmic Frontier: Astrophysical Instruments for the 21st Century, ESO Astrophysical Symposia Series, ed. A. P. Lobanov et al. (Berlin: Springer-Verlag), 179
Lestrade, J.-F., Preston, R. A., Jones, D. L., et al. 1999, A&A, 344, 1014
Lestrade, J.-F., Rogers, A. E. E., Whitney, A. R., et al. 1990, AJ, 99, 1663
Lister, M. L., Aller, H. D., Aller, M. F., et al. 2009, AJ, 137, 3718
Ma, C., Arias, E. F., Eubanks, T. M., et al. 1998, AJ, 116, 516
Marscher, A. P. 1998, in ASP Conf. Ser. 144, IAU Colloq. 164: Radio Emission from Galactic and Extragalactic Compact Sources, ed. J. A. Zensus, G. B. Taylor, & J. M. Wrobel (San Francisco, CA: ASP), 25
Pagels, A., Krichbaum, T. P., Graham, D. A., et al. 2004, in Proc. of 7th European VLBI Network Symp. on New Developments in VLBI Science and Technology, ed. R. Bachiller et al. (Madrid: Observatorio Astronòmico Nacional), 7
Pauliny-Toth, I. I. K. 1998, in ASP Conf. Ser. 144, IAU Colloq. 164: Radio Emission from Galactic and Extragalactic Compact Sources, ed. J. A. Zensus, G. B. Taylor, & J. M. Wrobel (San Francisco, CA: ASP), 75
Pauliny-Toth, I. I. K., Porcas, R. W., Zensus, J. A., Kellermann, K. I., & Wu, S. Y. 1987, Nature, 328, 778
Pradel, N., Charlot, P., & Lestrade, J.-F. 2006, A&A, 452, 1099
Ratner, M. I., Bartel, N., Bietenholz, M. F., et al. 2012, ApJS, 201, 5 (Paper V)
Schmidt, M. 1968, ApJ, 151, 393
Shapiro, I. I., Bartel, N., Bietenholz, M. F., et al. 2012, ApJS, 201, 1 (Paper I)
Shapiro, I. I., Wittels, J. J., Counselman, C. C., III, et al. 1979, AJ, 84, 1459
Snellen, I. A. G., McMahon, R. G., Hook, I. M., & Browne, I. W. A. 2002, MNRAS, 329, 700
Stickel, M., Meisenheimer, K., & Kuehr, H. 1994, A&AS, 105, 211
Vercellone, S., D'Ammando, F., Vittorini, V., et al. 2010, ApJ, 712, 405
Walker, R. C. 1999, in ASP Conf. Ser. 180, Synthesis Imaging in Radio Astronomy II, ed. G. B. Taylor, C. L. Carilli, & R. A. Perley (San Francisco, CA: ASP), 433